UNIVERSITY OF CALIFORNIA
RIVERSIDE

Polymeric Nanocomposites with Magnesium Oxide, Zinc Oxide, and Graphene Nanoplatelets Dopants for Tissue Engineering and Biosensing Applications

A Dissertation submitted in partial satisfaction
of the requirements for the degree of

Doctor of Philosophy

in

Material Science and Engineering

by

Dongwei Sun

September 2022

Dissertation Committee:

Dr. Huinan Liu, Chairperson
Dr. Iman Noshadi
Dr. Jianlin Liu

The Dissertation of Dongwei Sun is approved:

_____

_____

_____

Committee Chairperson

University of California, Riverside

Acknowledgments

Sincerely I would appreciate the effort and guidance from Dr.Huinan Liu during my Ph.D. research. Her support is significant to help me overcome all the difficulties in my Ph.D. study. I would like to thank the entire dissertation committee members: Dr. Huinan Liu, Dr. Jianlin Liu, Dr. Iman Noshadi for their kind insightful support and time commitment with my project and dissertation.

I would express thanks my oral committee members: Dr. Huinan Liu, Dr.Ashok Mulchandani, Dr. Sandeep Kumar, Dr. Jianlin Liu, and Dr. William H Grover for their guidance and advice with my research work. I would also like to thank all my previous and current labmates and visiting scholars, Wayne Leu, Patricia Holt-Torres, Changlu Xu, Yiqing Chen, Ruoyu Sheng, Dr.Chunyan Zhang, for their generous help.

I would like to thank all the staffs and professor in Material Science and Engineering Program and Bioengineering department and for their professional work and help. I would like to thank Nancy Ford, Hong Xu, Perry Chuang and Dr.Krassimir Bozhilov. Also, I would thank all the assistance from undergraduate students, Aaron Huang, Stephanie Cervantes, from NSF MacREU, Navy TUNE, NIH MARC U-STAR , and RICE program.

I want send my heartfelt thanks to my family. My parents, brother and sister are always so supportive of my pursuit for a PhD degree. They have always inspired and motived me to keep moving.

The rest chapters of this dissertation, in part or in full, will be presented in future publications. I would like to thank all the co-authors for their contributions.

ABSTRACT OF THE DISSERTATION

Polymeric Nanocomposites with Magnesium Oxide, Zinc Oxide, and Graphene Nanoplatelets Dopants for Tissue Engineering and Biosensing Applications

by

Dongwei Sun

Doctor of Philosophy, Graduate Program in Material Science and Engineering
University of California, Riverside, September 2022
Dr. Huinan Liu, Chairperson

Polymer nanocomposites are polymeric matrix doped with various nanomaterials (such as nanoparticles, nanotubes, nanoplatelets, and nanosheets), which could possess combined properties of polymer and nanomaterials. Some metal oxide nanoparticles (for example, magnesium oxide (MgO), zinc oxide (ZnO)), and carbon-based nanomaterials, such as graphene nanoplatelets (GnPs), have shown attractive features in biomedical applications. MgO and ZnO could serve as crosslinking agents in the polymeric matrix and provide enhanced mechanical properties. Meanwhile, they showed good antibacterial and antimicrobial activities and could be fully metabolized and resorbed in the body. GnPs exhibited outstanding mechanical strength and electrical conductivity.

This study focuses on the properties and potential applications of polymeric nanocomposites based on poly (glycerol sebacate) (PGS) elastomer doped with MgO, ZnO, and GnPs. We synthesized nanocomposites and investigated the influence on the performances of PGS elastomer. Our triphasic nanocomposites (PGS-GnPs-ZnO-MgO) showed improved mechanical strength and cross-linking density. The biphasic

nanocomposite (PGS-GnPs) with different GnPs contents from 25 wt.% to 0.1 wt.% exhibited various electrical performance and cytocompatibility. With high GnPs contents (above 10 wt.% of GnPs), the nanocomposites observed enhanced electrical conductivity, mechanical strength, and sensitive spiezoresistive behavior, which made these nanocomposites good candidates for strain sensor applications. The cytocompatibility evaluation through *in vitro* study with bone marrow stromal cells (BMSCs) indicated the dose-dependent toxicity of GnPs. With low GnPs contents (lower than 1 wt.%), the PGS-GnPs nanocomposites showed improved mechanical properties without reducing the adherence or proliferation of BMSCs, which showed great potential for polymeric scaffold applications.

Table of Contents

List of Figures

List of Tables

INTRODUCTION

Nanocomposites are materials that consist of multiple components and phases with various physical and chemical properties. According to matrix and dopant materials, nanocomposites could commonly be classified into ceramic nanocomposites, metal nanocomposites, and polymer nanocomposites [1]. Polymer nanocomposites are polymeric matrix doped with nanoparticles, nanorods, nanosheets, or nanoplatelets [2]. Those nanostructures with uniform distributions and interaction with the polymer matrices exhibit the combined properties of each component.

To achieve unique designated features of polymer nanocomposites, various nanostructures have been studied as dopants, including metal oxides [3], ceramic nanoparticles, and carbonaceous materials (e.g. carbon nanotube, graphene, and graphene nanoplatelets) [4]. The complicated interfacial regions and interactions between nano dopants and polymer matrix are critical for achieving the desirable properties (e.g. mechanical, electrical, and thermal).

Herein, in this study, we focused on investigating the influence of different nano dopants on the properties of polymer nanocomposite and exploring their potential applications. We first fabricated triphasic nanocomposites by incorporating magnesium oxide (MgO NPs), zinc oxide (ZnO NPs) nanoparticles, and graphene nanoplatelets (GnPs) into poly(glycerol sebacate) (PGS) matrices, which is a biodegradable elastomer. And characterized the distributions of the nano dopants, surface properties, mechanical properties, and biological properties of triphasic nanocomposites.

Secondly, we synthesized biphasic nanocomposites by doping various contents of GnPs into PGS matrices. The biphasic nanocomposites were fabricated into thin film via solvent casting methods and further charactered with mechanical, electrical, and biological properties. Further, we discussed the potential applications in tissue engineering scaffolds and physiological and motion signal monitoring applications based on the unique electrical and biological performance.

CHAPTER 1

Triphasic Polymer Nanocomposites with Graphene Nanoplatelets and Oxide Nanoparticles – Synthesis, Characterization, and Properties

Abstract

Nanocomposites, such as nanoparticles doped polymer matrix have shown promising applications in tissue engineering. In this study, we incorporated three nano dopants, magnesium oxide (MgO NPs), zinc oxide (ZnO NPs), and graphene nanoplatelets (GnPs) into poly(glycerol sebacate) (PGS), which is a biodegradable elastomer and investigated their mechanical and biological properties. Microstructural characterization confirmed that nanoparticles were uniformly dispersed in the composites. Compared with PGS elastomer, the incorporation of dopants increased the cross-linking density, which results in multi-folds of young's modulus, ultimate tensile strength, and modulus of elasticity. The sol content of PGS nanocomposites was greatly increased compared with PGS elastomer, which came with less degree of swelling. In addition, the electrochemical test showed a decreased impedance of the PGS elastomer by adding GnPs dopants. The study of 24-hour *in vitro* bone marrow-derived mesenchymal stem cells (BMSCs) showed a decreased BMSCs viability on PGS nanocomposites. The effects of nanoparticles on the proliferation of BMSCs showed a concentration-dependent behavior in vitro. Meanwhile, the groove pattern created on the surface of composite films exhibited cell alignment and guidance. This study provided explored a new strategy to synthesize PGS triphasic nanocomposites with different surface morphology and revealed the effects of dopants and surface patterns. The enhanced mechanical property, cross-linking density, electrical conductivity, and induced cell alignments are valuable for different biomedical applications.

Keywords: PGS nanocomposites, magnesium oxide, zinc oxide, graphene nanoplatelets, cytocompatibility

1.1. INTRODUCTION

Polymer nanocomposites have been attractive and extensively studied in the past years. As they exhibit better properties than traditional composites in terms of mechanical properties, thermal and dimensional stability, gas permeability, optical and electrical properties, etc. When nanofillers were introduced into a polymer matrix, their surface interaction, bonding, and dispersion with the polymer phase exhibited profound effects on the resulting properties of the polymer nanocomposites. Usually, the nanofillers show at least one of their dimensions in the nanoscale and can be classified into three major types one-dimensional, two-dimensional, and three-dimensional nanofillers, such as in the form of nanoplatelets, nanotubes, nanoparticles, etc [2]. Various nanofillers have been explored to alleviate the limitation of polymer and achieved unique tunable features.

Among them, metal oxide nanoparticles are promising three-dimensional dopants attributed to unique properties like high thermal stability, high chemical stability, biocompatibility, and high surface reaction activity, such as magnesium oxide (MgO NPs) and zinc oxide (ZnO NPs) nanoparticles. The MgO NPs are an inorganic salt of magnesium that can work as a ceramic phase and crosslinking agent in a polymer matrix. It had been found that MgO NPs dopants enhanced the mechanical and biological properties of the polymer matrix, such as PCL [5], PLLA [6], etc. The ZnONPs nanoparticle, as a semiconducting metal oxide, can exhibit a piezoelectrical response under mechanical deformation. Vinayak *et al*. found Polyaniline/ZnO NPs (PANI-ZnO) composites showed improved conductivity [7, 8]. Meanwhile, both MgO NPs and ZnO NPs nanoparticles could act as dose-dependent antimicrobial agents, which has shown excellent antibacterial

performance against bacteria and viruses [9-12]. As two-dimensional nanofillers, graphene nanoplatelets (GnPs) showed remarkable electrical conductivity and mechanical strength. GnPs dopants greatly enhanced the elastic modulus and conductivity in the polymer matrix, such as PCL, PLA, PU, etc [13].

In the case of biopolymers, a single type of nanofiller reinforcement of either metal oxide nanoparticles as ceramic phases or GnPs as conductive phases has been studied. In most cases, the reported results only focused on a single area of the properties of the composites. Another important aspect is the chemical interfacial interactions between the polymeric matrix and the nanofillers. Several works reported enhanced properties, however, it is still very different to interpret the interaction between fillers with the polymer. This is further complicated when introducing multiple nanofillers into the polymer matrix. So far, little attention has been paid to the comparative aspects of multiple phases in polymer nanocomposites.

Hence, this study aims to investigate the effect of MgO NPs, ZnO NPs, and GnPs nanofillers on the elastic modulus, sol-gel content, electrical conductivity, and cytocompatibility of a polymer matrix. Systematic comparative measurements were also carried out to interpret the interaction of multiple fillers. Meanwhile, exploring the influence of nano dopants and surface micro-texture on BMSC cytocompatibility is aimed at tissue engineering applications. In this study, we selected a biodegradable elastomer poly(glycerol sebacate) (PGS) as the matrix, which was first synthesized via polycondensation reactions between glycerol and sebacic acid by Wang et al. in 2002 [14]. As a soft elastomer, PGS has an average tensile Young's modulus in the range 0.0250 –

1.2 MPa, the ultimate tensile strength is > 0.5 MPa, and strain to failure greater than 330 % [14-16]. The solvent casting technique is a widely used method to synthesize polymeric composite in the laboratory, such as gelation methacryloyl [17], PCL[18], and collagens [19]. Hence, we used this method to prepare nanostructured triphasic (PGS/ MgO NPs/GnPs) composites and compare them to PGS elastomer, PGS/ MgO NPs, and PGS/ MgO NPs/ZnO NPs composites. Wetteland *et al*. found out that MgO NPs have an optimal effect on increasing BMSCs adherence density when cultured with a concentration of 200 µg/mL [20]. Considering the crosslinking strength and concentration-dependent antimicrobial effect, the mass of doped MgO NPs was calculated and yielded a 20 wt.% MgO NPs of PGS matrix (P80M20) [21]. The P80M20 composite was future doped with ZnO NPs and GnPs, to induce piezoelectricity and enhance the conductivity, respectively. As ZnO NPs have revealed a dose-dependent antimicrobial activity [22], the minimum inhibitory concentration of ZnO NPs was 40 µg/ml [23]. Increased cell death was observed with high concentrations of 50–100 mg/L [24], and co-doped ZnO lead to mitochondrial dysfunction and cellular membrane damage in the cells at the concentration of (0.5 mg/mL) [25]. Thus, the mass of ZnO NPs was calculated based on the concentration and yielded a 10 wt.% ZnO NPs of the composite matrix (P80M10Z10). The previous studies on GnPs doped polymers, such as PCL [13], polydopamine (PDA) with PCL [26], *etc*, have shown outstanding conductivity. In addition, some studies found out 1% single-layered Gr has the lowest cytotoxicity [27]. Thus 1wt.% GnPs were doped into the P80M20 matrix, to fabricate conductive polymer composite. The details of the sample composition were summarized in Table 1.

Table 1 Sample Compositions

Samples	PGS/Ethanol ratio (mg/ml)	Wt.% of PGS	Wt.% of MgO NPs	Wt.% of ZnO NPs	Wt.% of GnPs	Abbreviation
PGS elastomer	1: 1.5	100	0	0	0	PGS
PGS-MgO composite	1: 1.5	80	20	0	0	P80M20
PGS-MgO-ZnO composite	1: 1.5	80	10	10	0	P80M10Z10
PGS-MgO-GnPs composite	1: 1.5	80	19	0	1	P80M19G1
For abbreviation, "P" refers to PGS, "M" refers to "MgO NPs", "Z" refers to "ZnO NPs" and "GnPs" refers to graphene nanoplatelets.						

1.2. MATERIALS AND METHODS

1.2.1. Prepare Triphasic Nanocomposite and Controls

The PGS pre-polymer was purchased from the Secant Group, LLC (Regenerez®). The MgO NPs and ZnO NPs were purchased from US Research Nanomaterials Inc, which have diameters of 14 ± 3 nm and 40 ± 6 nm, respectively. The GnPs were purchased from Sigma-Aldrich (900412, Sigma-Aldrich), which has a particle size of around 5 μm, an average thickness of 6-8 nm, and a surface area ranging from 120-150 m^2/g, as shown in Fig. 1.1.

The nanoparticle-doped PGS composites were synthesized via solvent casting. The preparation of the P80M20 composite was briefly described below. Firstly, the PGS pre-polymer was dissolved in 100% ethanol with a weight-to-volume ratio of 1:1.5. The solution was placed in an Incu-shaker (Setting: 120 RPM; Benchmark Scientific) at 50 °C for 30 mins to accelerate the dissolving process. The MgO NPs (20 wt.%) were first dried

through heating at 200 °C in an oven for one hour to remove all the moisture content; then slowly added into a PGS pre-polymer solution to prepare a P80M20 suspension. A high-power sonicator was used to disperse P80M20 suspension (Model S-4000, Misonix) for 5 min with 5 s on and 5 s off mode to achieve a homogenous distribution. After sonication, the P80M20 suspension was placed in a dual asymmetric centrifugal mixer (speed mixer, FlackTek Inc) to remove the trapped bubbles, followed by degas process in a vacuum environment for 30 mins.

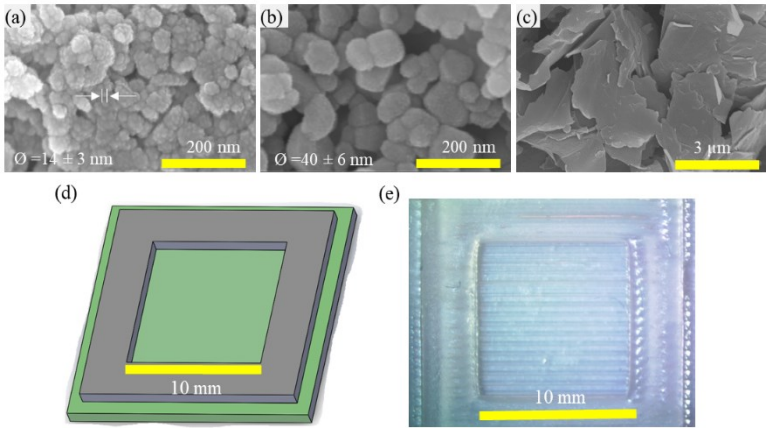

Fig. 1.1. Characterization of MgO NPs, ZnO NPs, and GnPs; shape and design of silicone mold, and optical images of the surface morphology of 3d printed silicone molds. (a), (b) and (c) are the SEM images showing the nanostructure of MgO NPs, and ZnO NPs at 250,000× magnifications, and GnPs at 20,000× magnifications, which found particle sizes of Ø14 ± 3 nm, Ø40 ± 6 nm, and around 5 µm, respectively. (e) shows the clear square silicone mold with 1 mm depth and parallel groove on the bottom surface.

Finally, the degassed P80M20 suspension was poured into a silicone mold, then cured at 120 °C for 48 h under vacuum conditions. Similar to the P80M20 composites, the preparation of other PGS nanocomposites followed the same procedure above. ZnO NPs (10 wt.%) and MgO NPs (10 wt.%) were added to PGS pre-polymer solution and the

composite was named P80M10Z10, while PGS nanocomposite with Gr (1 wt.%) and MgO (19 wt.%) was named P80M19G1.

1.2.2. Characterize Surface Morphology, Microstructure, Crystallinity, Elemental Composition, and Wettability

The surface morphology and features of PGS elastomer and PGS composites films were observed via optical microscopy and a field emission scanning electron microscope (SEM, Nova NanoSEM450, FEI). The surface profiles were scanned and generated using 3D laser scanning microscopy (VKX150, Keyence). The microstructure of the PGS elastomer and nanocomposites on the surface and cross-section was observed under SEM, meanwhile, the elemental compositions of PGS elastomer and nanocomposites were analyzed using energy-dispersive x-ray spectroscopy (EDS) with a 15kV accelerating voltage. All samples for SEM and EDS characterization were sputter-coated before observation with Pt/Pd using 20 mA for 60 seconds (Cressington, Sputter Coater 108 Auto).

The surface wettability was evaluated by water contact angles measured via a goniometer (type G16, Wet scientific). The crystalline phase structure of PGS elastomer and nanocomposites was determined by X-ray diffraction spectroscopy (XRD, PANalytical Empyrean Series 2) measurements. Data were collected over the range 2θ = 2° – 60° using a step size of 0.02° at a speed of 0.25° min^{-1}. These measurements allowed studying the homogeneity of the distribution of inorganic particles and exploring the metallic and organic bonds between PGS and nanoparticles. The attenuated total reflectance-Fourier transform infrared (FTIR-ATR) spectroscopy

(Thermo Scientific™ Nicolet™ iS10) was collected and analyzed using OMNIC software. The FTIR-ATR spectra were measured in the wavenumber range of 400-4000 cm^{-1}.

1.2.3. Analyze Thermal Properties via TGA and DSC

The thermal properties of PGS and PGS composites were evaluated with thermal gravimetric analysis (TGA) (Netzsch TG 209 F1 Libra) and a differential scanning calorimeter (DSC) (Netzsch DSC 214 Polyma). For TGA characterization, the PGS and PGS composites samples with a weight of approximately 3 mg were prepared and placed in alumina crucibles. A heating/cooling rate of 10 °C/min was applied from room temperature to 600 °C. For DSC measurement, samples with a mass of 40 μg were placed inside the aluminum concave pan and lid, and heated/cooled between – 40 and 100 °C, at a rate of 10 °C/min. All experiments (TGA and DSC) were performed under a nitrogen atmosphere. The melting (T_m) and recrystallization (T_c) temperatures were measured at the peak of the process. The glass transition (T_g) was defined by the mid-point inflection in the heat capacity curve.

1.2.4. Evaluate Swelling Behavior and Sol-Gel Contents

The sol-gel content of the PGS elastomer and nanocomposites network was evaluated via a swelling test in the organic solvent. Briefly, all samples were cut into strips of a size of 5 mm × 5 mm and immersed in tetrahydrofuran (THF) at 37 °C until they swelled to equilibrium. Each sample was weighed before immersion (W_{ini}), and after fully swollen (W_{swo}). The fully swollen samples were placed in an oven at 60 °C for 24 hours to evaporate all the solvent. The weight of the final dry samples (W_{dry}) was measured. The sol

content, gel content, and degree of swelling (DS) were calculated according to Eq. (1), (2), and (3) [28], respectively. For each group, swell tests were triplicated and repeated.

$$\text{Sol content (\%)} = (W_{ini} - W_{dry})/W_{ini} \quad \text{Eq.(1)}$$

$$\text{Gel content (\%)} = 1 - \text{sol content} \quad \text{Eq. (2)}$$

$$\text{Swelling (\%)} = (W_{swo} - W_{dry})/W_{dry} \quad \text{Eq. (3)}$$

1.2.5. Determine Mechanical Properties via Tensile and Three-Point Bending Testings

The mechanical properties of PGS elastomer and nanocomposites were measured through the tensile test and three-point bending test using an Instron 5969 Dual Column Testing System, following the ASTM D3039 and ASTM D790 standard test methods, respectively. The tensile test was conducted with a 500 N load cell at a constant displacement rate of 2 mm/min. The samples were proportionally cut into strips with sizes scaled down to 50 mm × 5 mm × 0.5 mm, according to the ASTM D3039 standard. All samples were elongated to failure. Young's modulus (E) and ultimate tensile strength (UTS) at break were extracted and plotted. Besides, the three-point bending test applied a 500 N load cell and a constant loading rate of 1mm/min. All samples had a size of 8 mm × 5 mm × 0.5 mm, and were deflected until a maximum strain of 5.0 % is reached. The flexural stress (σ_f), strain (ε_f), and modulus of elasticity (E) were calculated, according to equations (4), (5), and (6), respectively.

$$\sigma_f = 3PL/2bd^2 \quad \text{Eq. (4)}$$

$$\varepsilon_f = 6Dd/L^2 \qquad \text{Eq. (5)}$$

$$E = L^3m/4bd^3 \qquad \text{Eq. (6)}$$

Where: σ_f = stress at midpoint, MPa; ε_f = strain of strips, mm/mm; E = modulus of elasticity; P = load at a given point on the load-deflection curve, N; D = maximum deflection of the center of the strips, mm; m = slope of the tangent to the initial straight-line portion of the load-deflection curve, N/mm, L = support span, (mm); b = width of tested strips, (mm), and d = thickness of tested strips, (mm).

1.2.6. Measure Electrical Conductivity and Electrochemical Impedance

The electrical conductivity (σ) was calculated as the inverse of electrical resistivity, $\sigma = 1/\rho$, (ρ is the electrical resistivity) with a unit of siemens per meter (S/cm). The electrical resistivity is measured via a four-probe contact resistance station powered by a source meter (Keithley Instruments 2636, Cleveland OH) according to the equation. The probes were directly attached to the surface of the PGS elastomer and PGS composite film with a probe spacing is 0.5 mm between each other. The electrical resistivity (ρ_o) was described as Eq. (7).

$$\rho_o = (V/I) \times 2\pi sF \qquad \text{Eq. (7)}$$

Considering the geometries where the sample is semi-infinite in the lateral directions away from the probes, and that the sample thickness is greater than twice the probe spacing. A correction factor term was added to the original equation, as the sample thickness is approximately half the probe spacing, ($t \leqslant s/2$). The corrected equation is

modified as Eq. (8), which is now applicable for thin samples of semi-infinite lateral dimensions on a non-conductive substrate.

$$\rho = (V/I) \times \pi t/\ln(2) \qquad \text{Eq. (8)}$$

where: V is the voltage differential, I is the current passing through the sample, s is the probe spacing, F is a geometry correction factor, and t is the thickness of samples.

The electrochemical impedance spectroscopy (EIS) test was conducted using a potentiostat (Interface 1010E, Gamry instruments) in revised simulated body fluid (rSBF) at pH 7.4 and 37.5 °C. The EIS tests were conducted via a three-electrode cell configuration, which consisted of a reference electrode (Ag/AgCl), a counter cathode (platinum foil), and a working anode ("PGS elastomer" and "PGS composites" samples). All test specimens were cut into 10 mm × 10 mm squares and immersion the same depth. The preparation and composition of rSBF were described in previous work [ref]. The scanning started immediately when the working electrodes were immersed in the electrolyte.

1.2.7. Determine The Cytocompaibility of Nanocomposites via *in vitro* Culture with Bone Marrow-Derived Mesenchymal Stem Cells (BMSCs)

1.2.7.1. Prepare BMSCs Cell Culture

Rat BMSCs were extracted from the femur and tibia of juvenile Sprague Dawley rats according to the established protocol approved by the Institutional Animal Care and Use Committee (IACUC) at the University of California at Riverside. Briefly, the ends of the dissected long bones were cut using a scalpel and cell-containing bone marrow was

flushed out of the marrow cavity using Dulbecco's Modified Eagle Medium (DMEM; Corning) supplemented with 10 v/v % fetal bovine serum (FBS; Hyclone) and 1 v/v % penicillin/streptomycin (P/S; Hyclone). Hereafter, DMEM with 10 v/v % FBS and 1 v/v % P/S will be referred to as DMEM. The bone marrow was collected into a sterile 15 mL tube with DMEM and large clusters were broken up using a syringe. The cell suspension was then filtered using a 70 lm nylon strainer (Fisher Scientific, FisherbrandTM 22363548) to remove aggregates. The filtered cells were centrifuged and cultured in fresh DMEM in a T-75 flask under standard cell culture conditions (that is, a sterile, 37 °C, 5% CO2/95% air, humidified environment). After 3 days, the media was changed to wash away non-adhered hematopoietic stem cells, leaving only the adherent mesenchymal stem cells to be cultured until they reached confluency. The pH of DMEM was adjusted to 7.4 before being used in cell culture and the addition of MgO nanoparticles. BMSCs at their second passage were used for in vitro experiments with MgO nanoparticles. All the experimental procedures were conducted under sterile conditions using a biosafety II laminar flow hood (Class II Type A2, Labconco) and a cell culture incubator (MCO-19AIC, Sanyo Scientific) in a certified cell culture room.

1.2.7.2. Prepare Triphasic Nanocomposites and Controls For BMSCs Culture

To investigate the cytocompatibility of PGS elastomer and PGS composites with BMSC, meanwhile, to examine the cell growth guidance effect of pattern on bot surface, two groups of PGS elastomer and PGS composites samples were placed in the wells, either top surface facing up, and named as P80M19G1, P80M10Z10, P80M20, and PGS; or were bot surface facing up, named as P_P80M19G1, P_80M10Z10, P_P80M20, and P_PGS.

According to the actual amount of dopant of PGS composite, the dopants were also co-seeding with BMSC as control groups, including 10 % MgO NPs (n_M10), 10 % ZnO NPs (n_Z10), 20 % MgO NPs (n_M20), 1 % Gr nanoplatelets (n_Gr1), 19% MgO NPs and 1% Gr nanoplatelets (n_M19Gr1), 10 % MgO NPs and 10 % ZnO NPs (n_M10Z10). BMSCs were seeded at a density of 10,000 cells/cm^2 in a 12-well tissue culture-treated plate (Corning, Falcon, 353043) with 3 mL DMEMs added to each well. The PGS elastomer and PGS composites were pre-treated to remove the unreacted monomers.

1.2.7.3. Characterize Post-culture BMSCs and analyze media

After 24 h cell culture, the 3 mL DMEMs media was collected for post-culture analysis, and the non-adherent BMSCs were washed away using phosphate-buffered saline (PBS). The rest adherent BMSCs cells were fixation using 4% paraformaldehyde (Electron Microscopy Sciences, 15714-S), then stained with 4',6-Diamidino-2-Phenylindole (DAPI; Life Technologies) for the nuclei of the cells and Alexa Fluor 488-phalloidin (Life Technologies) for F-actin. The stained cells in each well were imaged using a fluorescence microscope (Nikon Eclipse Ti-S) at 10 random locations. BMSC were counted and adhesion density was calculated as the number of adhered cells per unit area.

The pH of the post-culture media was measured immediately after collection using a pre-calibrated pH meter (Symphony SB70P, VWR). The ion concentrations (Mg^{2+} and Ca^{2+}) were measured using an inductively coupled plasma optical emission spectrometry (ICP-OES; PerkinElmer Optima 8000). The Mg^{2+} and Ca^{2+} solution standards with ranges

of 0.5–5.0 and 0.1–1.0 mg/L are from Perkin Elmer. All the experimental and control groups were run in triplicate.

1.3. RESULTS

1.3.1. Surface Topography, Microstructure, Elemental Composition, and Wettability of Triphasic Nanocomposites and Controls

The PGS elastomer and nanocomposites samples were synthesized and cured in the oven. Their morphology and elemental composition of the top surface, cross-section surface, and patterned bot surface were analyzed by SEM and EDS, as shown in Fig. 1.2.

The top surface of each sample exhibited different characters. PGS elastomers had a smooth and concave surface, while PGS composites had a rough dendrite pattern which could be attributed to the agglomerations of nanoparticles in the matrix. The bot surface of each sample was rough as samples were peeled off from the patterned silicon mold. From the cross-section, the PGS elastomer shows a clean and smooth surface. The dopants of the PGS composites were identified and circled. The EDS analysis of the top surface, bot surface, and cross-section were shown in Fig. 1.2(e). It was found the Mg and Zn elemental composition had an increasing trend from the top surface to the bot surface, due to the sediment of nanoparticles during curing.

The macroscope images of patterned bot surface and 3D laser scanned morphology were presented in Fig. 1.3. All the samples were engraved with straight and parallel grooves on the surface. These grooves had a width and depth approximate of 600 and 90 μm,

respectively. A surface profile was scanned and generated in Fig. 1.3 (a2)-(d2), which revealed each groove had similar peaks and contours.

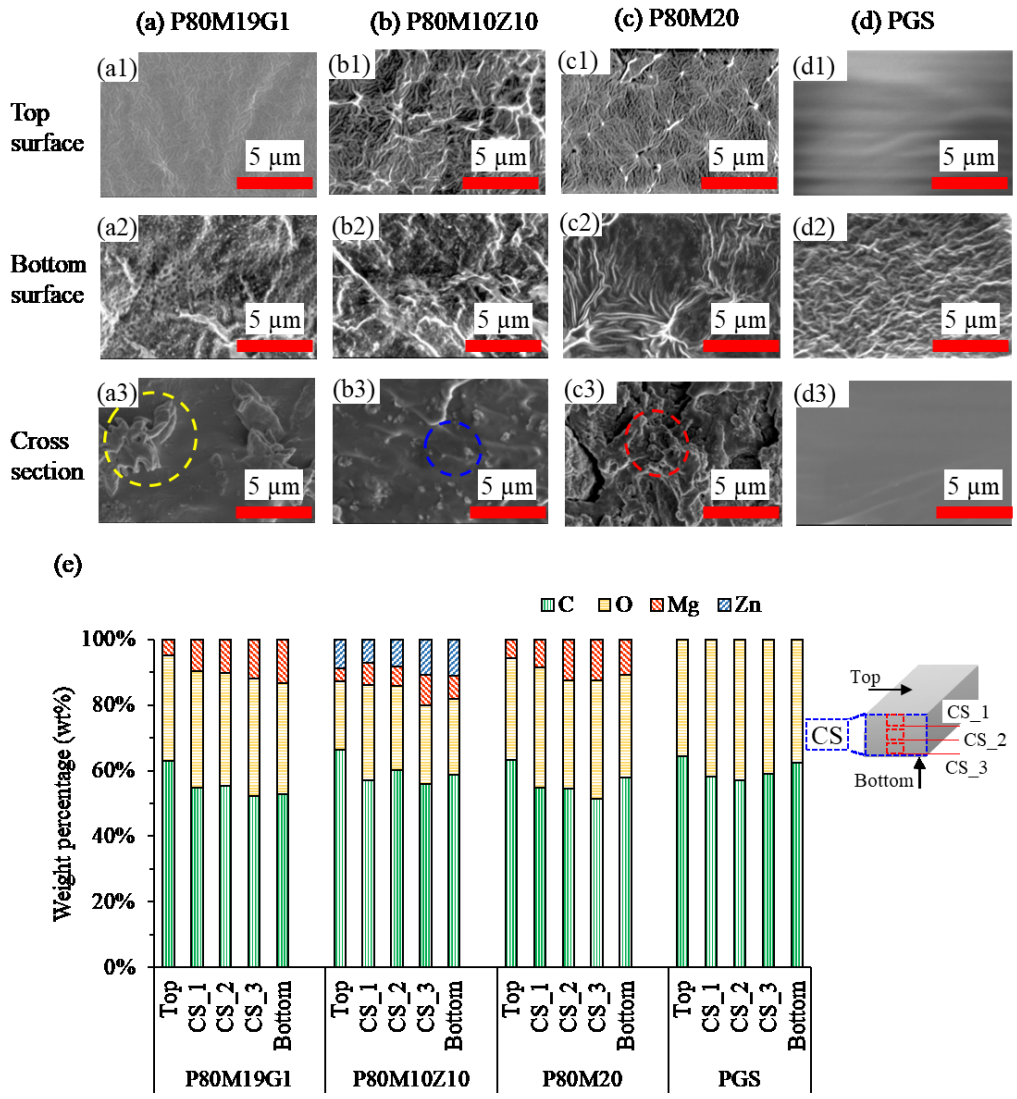

Fig. 1.2. Characterization of the microstructure, surface morphology, and element compositions of the PGS nanocomposites and PGS elastomer. (a)-(d) are SEM images that show the microstructure of the top surface, cross-section, and bottom surface for P80M19G1, P80M10Z10, P80M20, and PGS elastomer at original 10,000× magnification, respectively. The yellow dash circle indicates the GnPs cluster, the blue dash circle indicates ZnO NPs, and the red dash circle indicates MgO NPs. (e) the plots weight percentage of C, O, Mg, and Zn elements. Three different areas are chosen on the cross-section of the samples from top to bottom, marked as CS_1, CS_2, and CS_3.

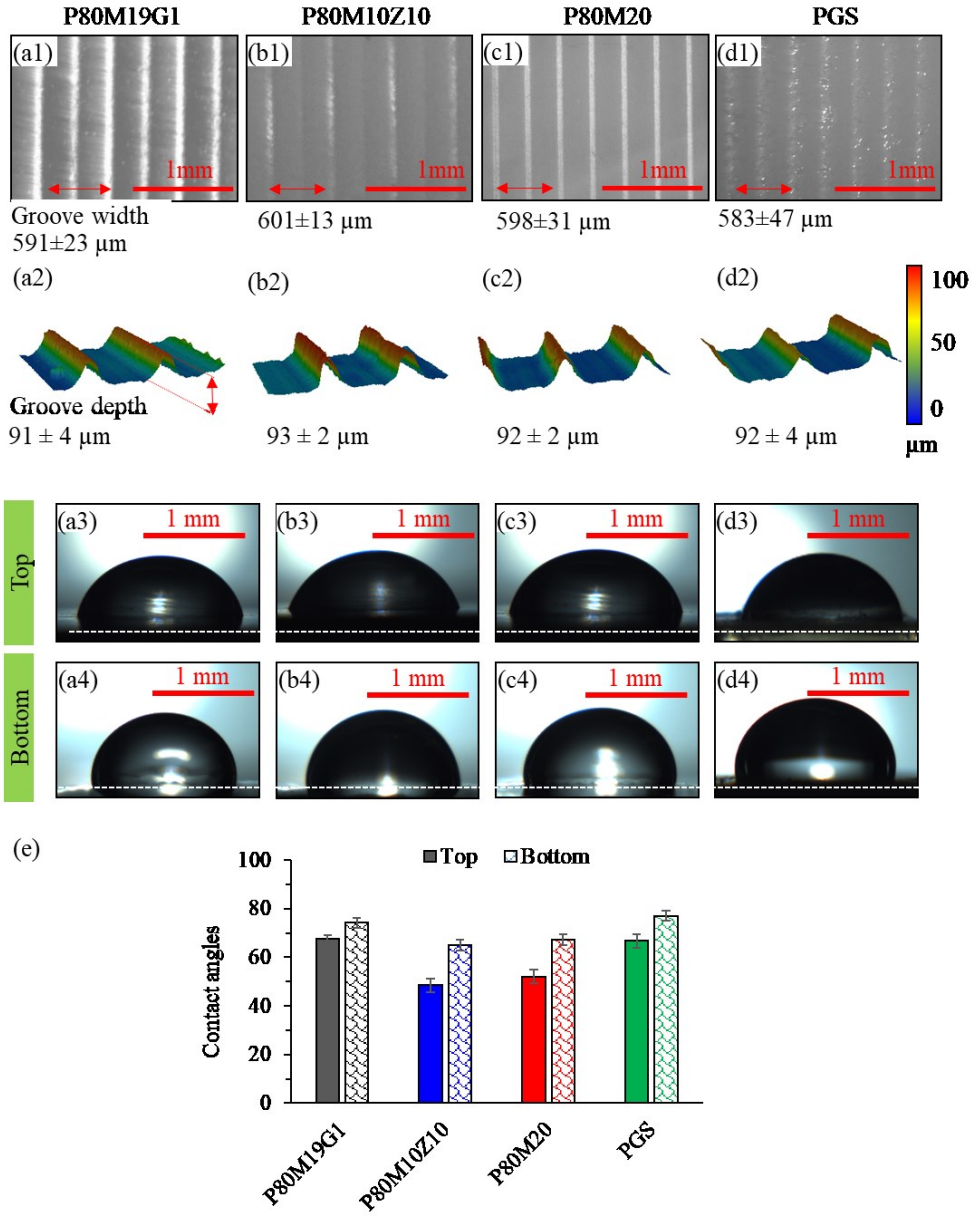

Fig. 1.3. Characterization of surface patterns and wettability of PGS nanocomposites and PGS elastomer. (a1)-(d1) laser scanning images represent the parallel grooves on the bottom surface, and (a2)-(d2) show the corresponding 3D scanned profile. The optical image of water droplets on the top surface and bottom surface are shown in (a3)-(d3) and (a4)-(d4). The contact angles were measured and plotted in (e).

The hydrophilicity of a material is a property that controls protein deposition, cell affinity, and degradation rate. The water contact angle of PGS elastomer and PGS composites were shown in Fig. 1.3(c). The material surface wettability is an important property for tissue engineering. The PGS polymer film showed poor hydrophilicity with a contact angle of 93 ± 0.35º. When 20 wt.% MgO NPs were introduced into PGS, and the water contact angle of the scaffolds increased to 102.43 ± 0.12°. On the other hand, the ZnO NPs and GnPs reduced the contact angle to 82 ± 0.7° and 71 ± 0.22°, indicating an increase in hydrophilicity of nanocomposites. The increase in hydrophilicity was likely due to the polyions present on the composite surfaces that attracted water molecules [29].

1.3.2. Crystallinity, Chemical Bondings, and Cross-Linking of Triphasic Nanocomposites and Controls

The nanoparticle dopants of the PGS composite and the bonding were identified by the FTIR (Fig. 1.4(a)), also the XRD spectrum confirmed that poof PGS elastomer and composite be semi-amorphous (Fig. 1.4(b)). The FTIR-ATR spectrum of PGS elastomer, PGS composites, and nanoparticles was illustrated in Fig. 1.4. Concerning the PGS sample, a broad absorption peak was observed around 3520 cm^{-1}, which was attributed to the hydrogen-bonded hydroxyl group (–OH) stretch vibration. The intense peaks in the range of 2927–2854 cm^{-1} were associated with alkene groups ($–CH_2$). The sharp peaks at 1735 cm^{-1} and 1172 cm^{-1} indicated the formation of ester bonds C=O and C–O, respectively [30, 31]. The peak at 1416 cm^{-1} was assigned to the carboxylic acid group (O–H) bend, while the peak at 940 cm^{-1} was the O–H stretch. The two peaks observed on PGS spectra at 1291 cm^{-1} and 1218 cm^{-1} were assigned to the stretching of C–O groups [36]. while CH_3 bend

appeared at 1378–1456 cm^{-1}. The carbonate stretching is also observed around 1600 cm^{-1}. The bands that appeared at low frequencies between 836 and 652 cm^{-1}correspond to stretching vibrations of Mg–O–Mg bonding [12, 32-34].

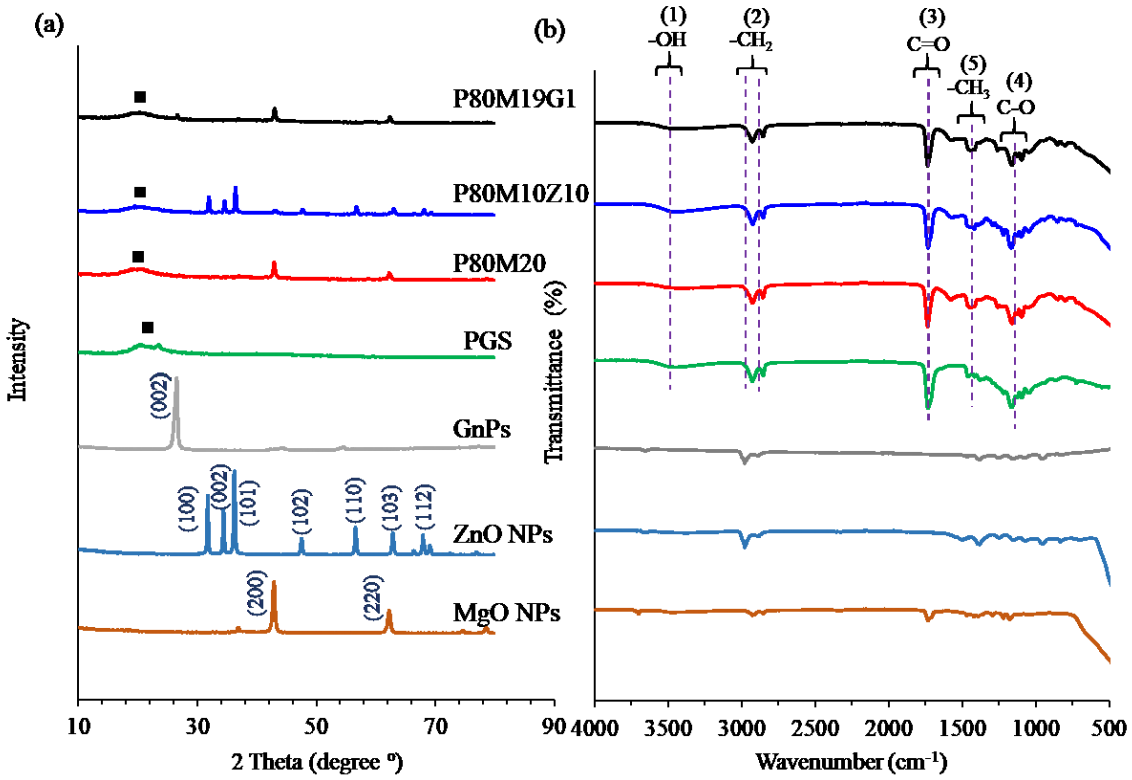

Fig. 1.4. Phase composition and chemical bonding of PGS nanocomposites and PGS elastomer. (a) XRD spectrum and (b) FTIR-ATR spectrum of PGS nanocomposite and elastomer. In XRD plots, the black squares "■" indicate wide diffractions of PGS from 15° to 23.6° with a peak at 2θ of 20.8°. In FTIR plots, (1) 3500-3200 cm^{-1}, hydroxyl (–OH) group; (2) 2927–2852 cm^{-1}, alkene ($–CH_2$) group; (3) and (4) at 1735 and 1159 cm^{-1} were ester group(C=O and C–O. (5) 1354–1456 cm^{-1}, methyl ($–CH_3$) bending.

Compared with the spectrum of PGS elastomer, PGS composites showed new peaks between 1510 and 1572 cm^{-1}, which were attributed to the stretch of magnesium and zinc carboxylates [35]. Those existing metallic carboxylates confirmed the reaction of metallic nanoparticles and PGS pre-polymer during PGS composite synthesis.

$$2\,(–COOH) + MgO \rightarrow (–COO^{–})_2\,Mg^{2+} + H_2O \qquad \text{Eq. (3)}$$

$$2\,(–COOH) + Mg^{2+}(OH^{–})_2 \rightarrow (–COO^{–})_2\,Mg^{2+} + 2H_2O \qquad \text{Eq. (4)}$$

PGS elastomer has a broad peak around $2\theta = 21°$, which indicated PGS elastomer has low crystallinity. The Gr nanoplatelets show a characteristic peak at $2\theta = 26.7°$, and two minor peaks at $2\theta = 45.7°$ and $2\theta = 55.8°$ are due to the impurities. MgO NPs show characteristic crystalline peaks at $2\theta = 42.89°$ (200) and 62.27° (220). For ZnO NPs, the diffraction peaks located at $2\theta = 31.61°$, 34.26°, 36.10°, 47.37°, 56.40°, 62.68°, and 67.72° correspond to the (100), (002), (101), (102), (110), (103), and (112) reflection planes of hexagonal structure of ZnO, respectively. The diffraction peaks of those MgO NPs, ZnO NPs, and GnPs were identified in the PGS composites, respectively. Compare XRD results of the PGS elastomer and P80M20, the MgO peaks of the P80M20 composite shift left due to the chemical interaction between PGS and MgO NPs. The interactions were further analyzed by FTIR-ATR spectroscopy.

1.3.3. Decomposition and glass transition temperature triphasic nanocomposites and controls

The influence of the nanoparticles on the elastomeric matrix thermal properties was characterized by thermogravimetric analysis (TGA) in Fig. 1.5(a). For PGS elastomer, the TGA curve showed a three stages decomposition. The first stage was around 100 °C, there is a minor weight loss due to the removal of the moisture. The second stage started around 290 °C to 420 °C, which was the partial decomposition of the PGS elastomer. A significant weight loss took place at 420°C due to the decomposition of the PGS chain backbone. The

chain with low molecular weight underwent degradation at a lower temperature. The PGS composited showed a four stages decomposition. The first stage around 100 °C indicated the removal of moisture. The mass loss of the second stage, third stage, and the fourth stage could be a partial decomposition of PGS, long metal-organic chain (high chelating density), and short metal-organic chain (low chelating density). Above 420 °C, the mass loss is due to the PGS chain backbone decomposition. The thermal stability of 20 wt.% weight MgO NPs reinforced PGS showed lower thermal stability than the pristine PGS elastomer. This could be attributed to the dissociation of inter and intramolecular hydrogen bonding in PGS [33] [6]. Finally, the sample residual weight of PGS nanocomposites was as indicated at 550 °C, the residual weight showed good consistency with the masses of the added fillers.

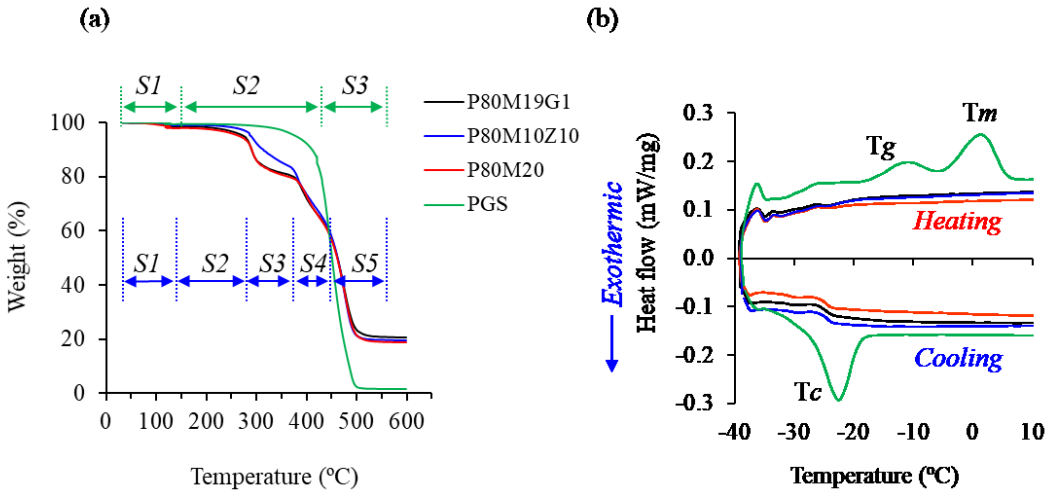

Fig. 1.5. Thermal properties of PGS nanocomposites and PGS elastomer. (a) Thermogravimetric profiles and (b) differential scanning calorimetry curves of PGS-nanocomposites and pristine elastomer. The TGA curve indicated a decomposition temperature starting slowly from 300 °C, and the DSC curves revealed a glass transition around −22 °C, followed by a melting transition of around 1.3 °C.

Differential scanning calorimetry (DSC) performed on the pristine and nanocomposite PGS samples were shown in In Fig. 1.5(b). PGS elastomer exhibited strong endothermic peaks (T_m) at 2.3 °C and a broad transition between −30 °C and −10 °C. The T_g was calculated as the midpoint of the slope, around −20.5 °C. During the cooling cycle, the PGS elastomer showed a strong exothermic peak at −23.5 °C, which is the crystalline temperature (T_c). The exothermic peaks T_c during the cooling cycles and endothermic peaks T_g and T_m during the heating cycles indicate that PGS elastomer is semi-crystalline below T_m, but soft and amorphous at 37 °C [8] [50]. The P80M19G1, P80M10Z10, and P80M20 composites showed T_g values of −27.2°C, −27.5°C, and −29.1°C, respectively. However, no obvious endothermic peaks (T_m) and exothermic peaks (T_c) of PGS composites were observed. Compared with PGS elastomers, the glass transition regions of PGS composites shifted to the left.

1.3.4. Sol-gel contents and swelling in THF

The swelling results for PGS elastomer and PGS composites were showed in Fig. 1.6. The sol-gel contents were calculated according to the weight of each sample. The sol content is composed of an uncross-linked macromer, which represents the crosslinking density of PGS elastomer and PGS composites. The PGS elastomer showed high sol content up to 58.9%, and a degree of swelling of 3097.9 %. The highly swollen PGS elastomer is easy to generate leachate in the THF medium. The PGS elastomer absorbs plenty of THF medium and expanded in width and thickness up to one fold. Compared with PGS elastomer, the PGS composites showed extreme reductions in sol content degree of swelling and expansion. The sol content of P80M19G1, P80M10Z10, and P80M20

samples decreased to 2.4%, 6.5%, and 4.8%, respectively. Meanwhile, the degree of swelling of P80M19G1, P80M10Z10, and P80M20 samples dropped to 72.0%, 89.1%, and 84.9%. As shown in Fig. 1.6(a), the PGS composites samples barely had size and volume expansion after immersion in the THF medium. These results indicated the incorporation of nanoparticles effectively increased the crosslinking density of PGS composites.

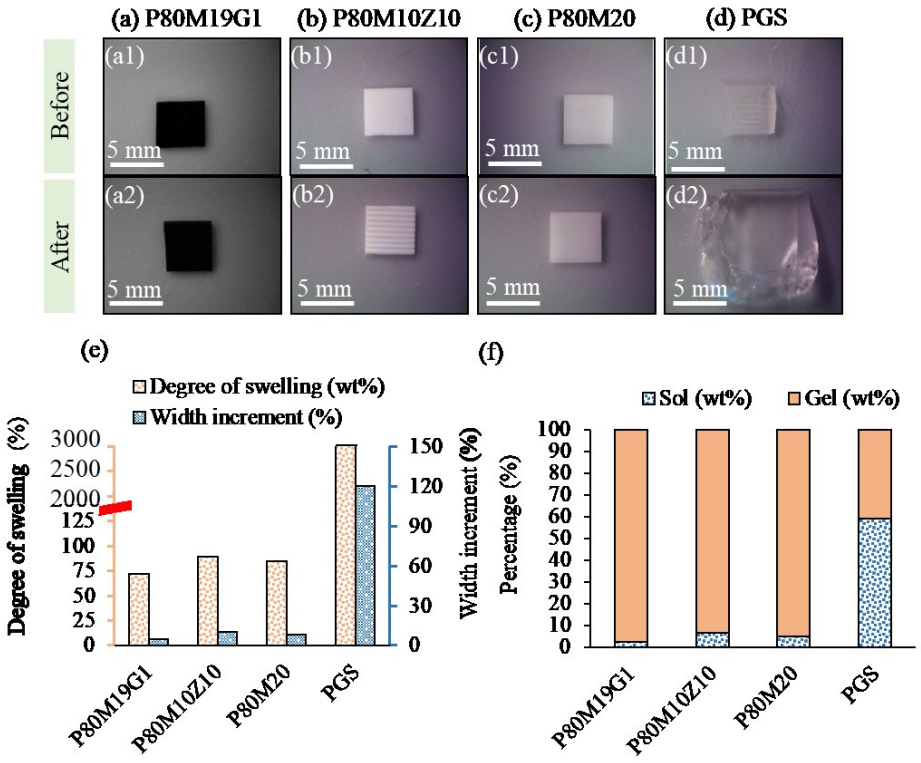

Fig. 1.6. Sol-gel content and volume change of PGS nanocomposites and PGS elastomer after immersion in THF. (a)-(d) are OM image represents the appearance and volume changes before and after swollen in THF. (e) showed the degree of swelling and width increment; (f) indicated the sol-gel content

1.3.5. Mechanical Properties of Triphasic Nanocomposites and Controls

The tensile stress-strain curve of PGS elastomer and PGS composites were typical of elastomeric behavior at room temperature, as shown in Fig. 1.7(a). The PGS elastomer showed ultimate tensile strength (*UTS*) and tensile modulus of elasticity (*E*) with values of 0.26 ± 0.03 and 1.1 ± 0.04 MPa. Significant improvements in UTS and E were found with nanoparticle incorporation.

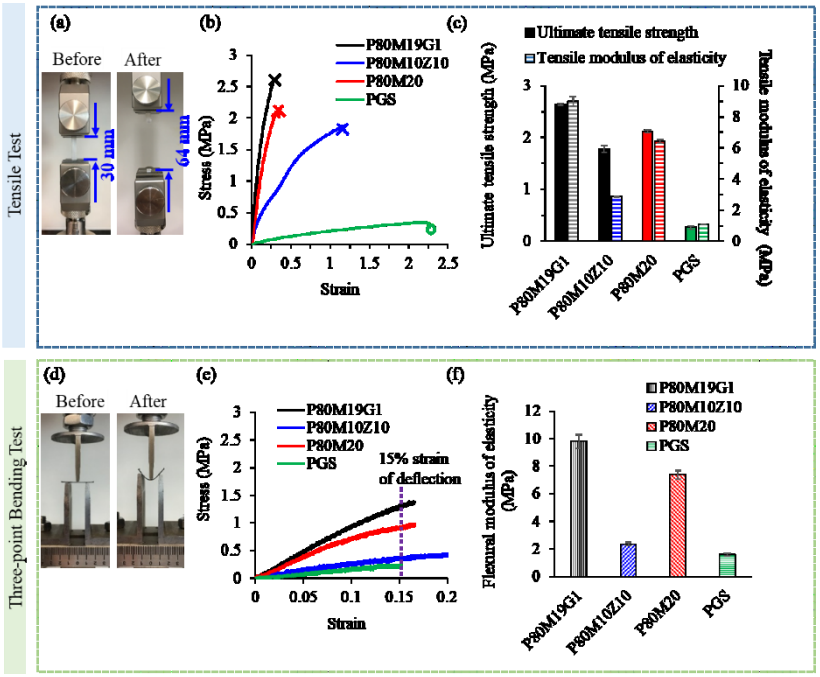

Fig. 1.7. Characterization of mechanical strength of PGS nanocomposites and PGS elastomers. (a) and (d) indicate the instrument setup for the tensile test and three-point bending test, respectively. (b) showed the stress versus strain curve during tensile testing and (c) plots the ultimate tensile strength (*UTS*) and tensile modulus of elasticity (*E*). The *UTS* values are 2.63 ± 0.02 , 1.45 ± 0.06, 2.12 ± 0.03, and 0.26 ± 0.03 MPa for P80M19G1, P80M10Z10, P80M20 and PGS respectively. The *E* values are 8.9 ± 0.28, 2.85 ± 0.02, 6.43 ± 0.13, and 1.1 ± 0.04 MPa for P80M19G1, P80M10Z10, P80M20 and PGS respectively. (e) showed a stress vs. strain behavior during bending, (f) plotted the flexural modulus of elasticities. The *E* values are 9.80 ± 0.5, 2.35 ± 0.12 , 7.39 ± 0.29 , and 1.59 ± 0.1 MPa for P80M19G1, P80M10Z10, P80M20 and PGS respectively. The modulus was determined using Hooke's law from the slope of the linear portion of the stress-strain curve, whereas the UTS was determined as the highest stress that a nanofiber sample could bear without breaking.

The P80M19G1 samples showed the highest values of 2.63 ± 0.02 and 8.9 ± 0.28 MPa, which are 4.9 and 34.4 times larger than the PGS elastomer. The P80M20 samples exhibited values of 2.12 ± 0.03 and 6.43 ± 0.13, which were slightly lower than the P80M19G1 samples. The ZnO filler of P80M10Z10 samples decreased both values of P80M20 samples to 1.45 ± 0.06, and 2.85 ± 0.02 MPa. However, these values were still 2.7 and 10.9 times higher than those of PGS elastomer. Nevertheless, the increase of filler content in the PGS matrix resulted in a decrease in the total elongation of the nanocomposites.

The flexural strength and modulus results were shown in Fig. 1.7(b). The P80M19G1 composite had the highest modulus of 9.80 ± 0.5 MPa, which is 6.19 folds of PGS elastomer with a value of 1.59 ± 0.1 MPa. The P80M20 samples showed less stiff values of 7.39 ± 0.29 MPa than the P80M19G1 samples. The ZnO NPs filler of P80M10Z10 reduced the value to 2.35 ± 0.12 MPa.

1.3.6. Electrical Conductivity and Impedance

The electrical conductivity and impedance of PGS elastomer and PGS composites were plotted in Fig. 1.8, P80M19G1 composites had the highest electrical conductivity of the other samples. Compared with PGS elastomer, the MgO and ZnO NPs fillers increased the electrical resistance.

The Nyquist plots of PGS elastomer and PGS composites, as shown in Fig. 1.8 (b), (c), and (d), exhibited consecutive semicircles, each of which was followed by a tail formation at a low-frequency region. The results showed impendence was stable and

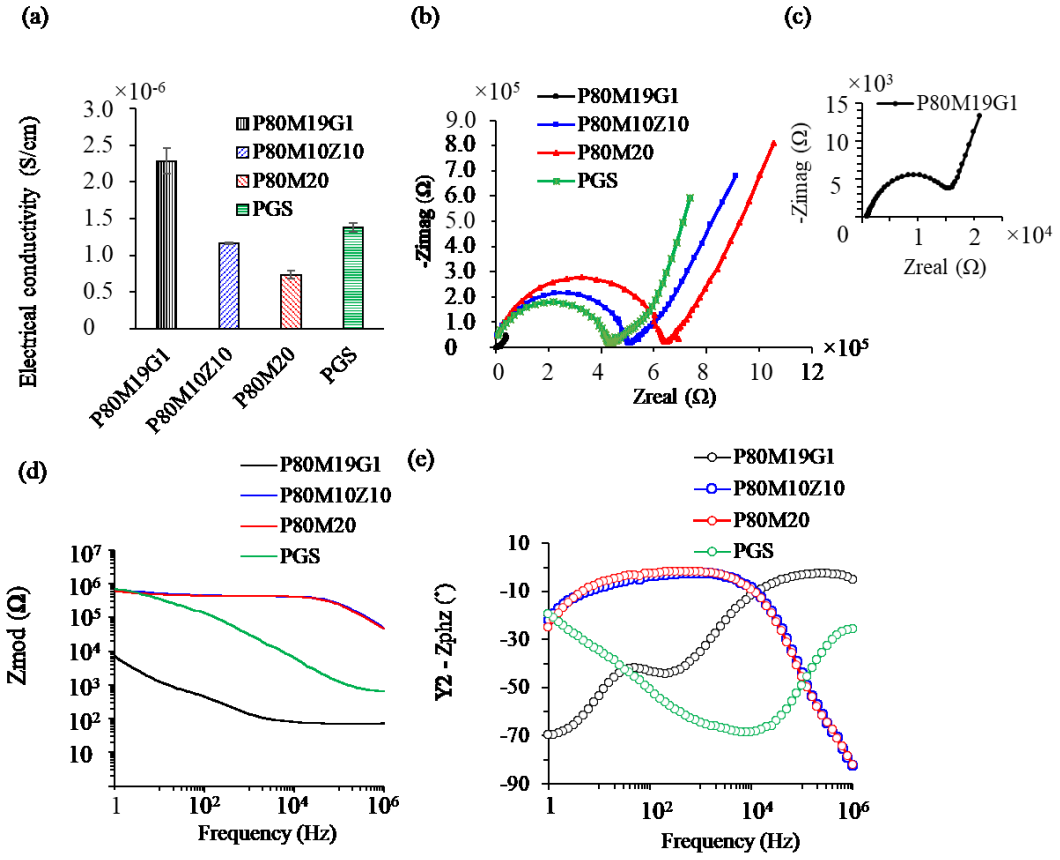

Fig. 1.8. Evaluation of electrical properties PGS nanocomposites and PGS elastomer. (a) electrical conductivity results of PGS nanocomposites and PGS elastomer measured using a four-probe station. (b-f) indicate EIS test results of PGS nanocomposites and PGS elastomer, and Mg plate (97% Mg, AZ31B): (b-c) Nyquist plot and (d-e) Bode plot;

distinguished at higher frequencies 10^4-10^6. The semicircle is related to the bulk composite and interface region between PGS composites and the medium, while the tail-like formation represents diffusion in the medium. As shown, the Mg control sample had the minimum impedance. P80M19G1 had a slightly higher value than that of Mg control, but a much smaller impendence value than other PGS elastomer and PGS composites. The GnPs decreased the impedance amplitude by almost two orders of magnitude. The Bode

Plots of PGS elastomer and PGS composites were shown in Fig. 1.8 (e) and (f). The MgO and ZnO nanoparticles greatly increased the impedance, compared with pure PGS elastomer. Due to the superior conductivity, the composite with Gr has exhibited a very low impedance of 7.07 kΩ, even close to the Mg control sample. This value is smaller than the reported impedance value of PPy (15 kΩ, 1kHz) [36].

1.3.7. BMSC Morphology, Adhesion Density, and Post-Culture Media Analyses

The morphology and density of BMSCs cultured with PGS elastomer and nanocomposites were characterized using fluorescence microscopy, as shown in Fig. 1.9. The BMSCs viability of PGS composites was significantly reduced when compared with PGS elastomer. Surviving cells exhibited abnormal morphology, appearing smaller and exhibiting signs of possible membrane damage. For the patterned surface samples, cell growth was well aligned straight along the groove.

The BMSC adhesion density was quantified based on the fluorescence images. In the control group, the cell density significantly increased after the cells were incubated with MgO and ZnO NPs for 24 h when compared with all the other BMSC and Glass groups. No statistical difference was detected when compared with n_M10 and n_Z10 or n_M20 and n_M19G1.

The addition of nanoparticles in PGS composites and DMEM showed similar effects on the media pH, Mg^{2+} concentration, and Ca^{2+} concentration under acellular conditions. As the MgO concentration increased, the media pH and Mg^{2+} concentration showed increasing trends.

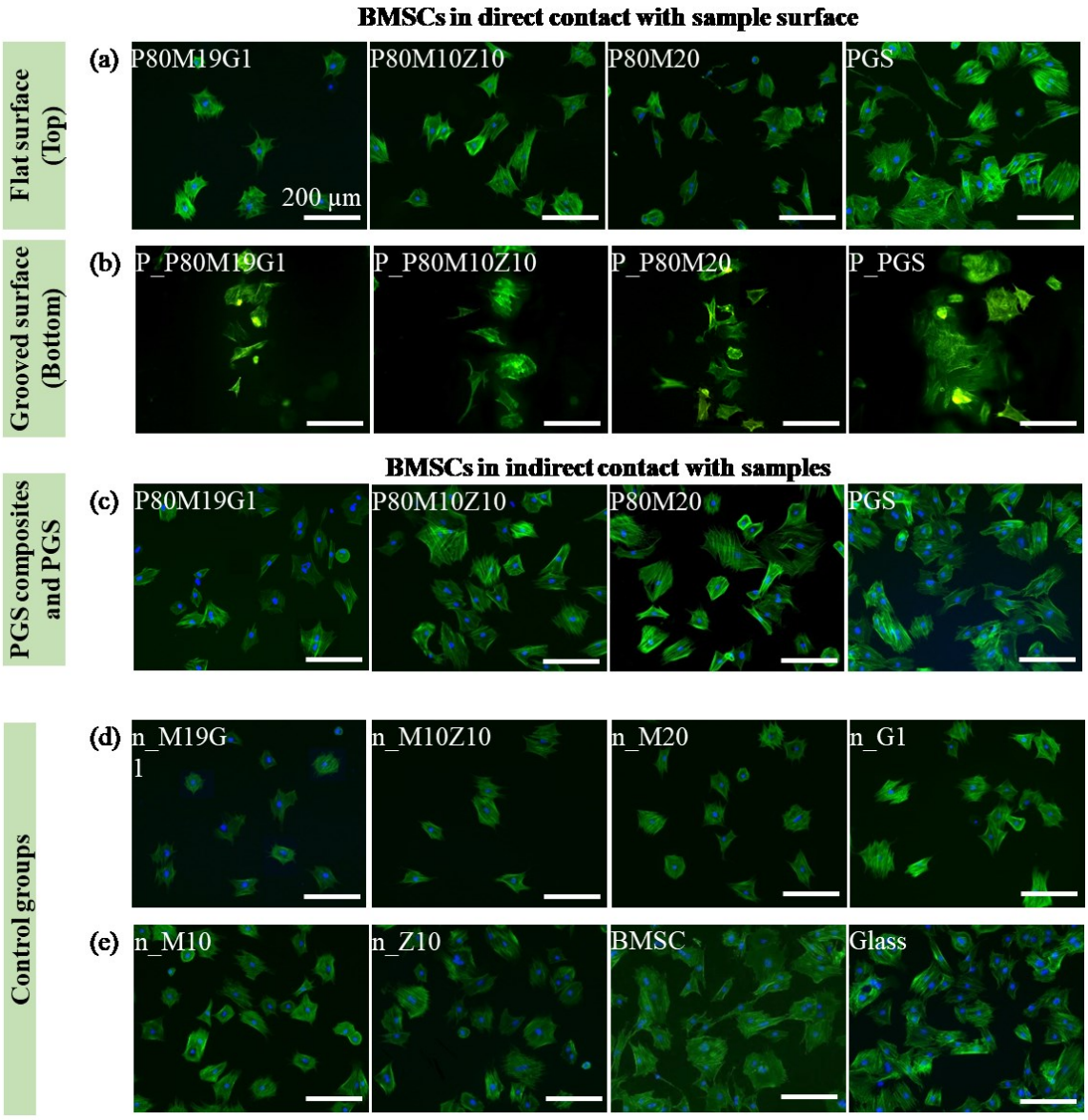

Fig. 1.9. Analysis of BMSCs cytocompatibility with PGS elastomer and nanocomposites in DMEM for 24 h. Fig. (a), (b), and (c) indicates the fluorescence images of BMSC adhesion and morphology on the top flat surfaces (direct contact), the bottom grooved surface of samples (direct contact), and the surface of the well surrounding the samples (indirect contact) after in vitro culture for 24 h, respectively. Fig. (d) and (e) indicated the BMSC adhesion and morphology with control samples. The original magnification is 100x, The scale bar is 200 µm. F-actin of BMSCs has been stained with Alexa Fluor 488 phalloidin as indicated in green color. BMSCs nucleus was stained with DAPI as indicated in blue color.

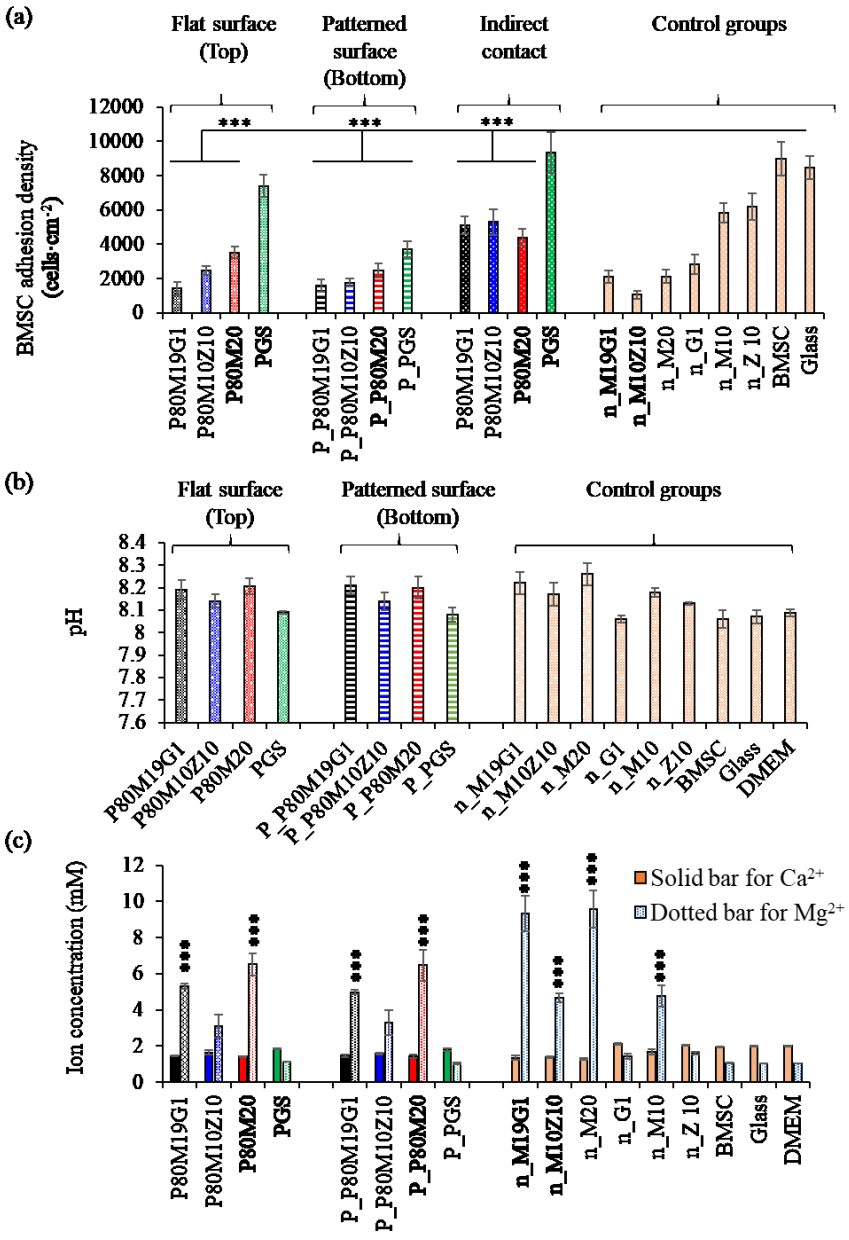

Fig. 1.10. Quantitative analyses of adhesion of BMSCs and post-culture media analysis. Fig. (a) plots the adhesion density of BMSCs under indirect contact and direct contact conditions. (b) pH and (c) Ca^{2+} ion and Mg^{2+} ion concentrations and in the media after 24-h direct culture of BMSCs with the samples and controls. The values of pH and ion concentrations were the average of media of triple wells. *p < 0.05, **p < 0.01, ***p < 0.001 when compared with the BMSC control.

1.4. DISCUSSION

1.4.1. Strengthening Mechanisms in the Composites

The PGS elastomer showed a high elongation at break but low values of strength and tensile modulus of elasticity. The incorporation of nanoparticles greatly increased the strength and modulus in the tensile test and 3 points bending test. The enhanced modulus and strength of the PGS nanocomposites could be attributed to several reasons. Firstly, the main cross-linking mechanism of the PGS pre-polymer is the formation of an ester bond via a condensation reaction between carboxylic acid and alcohol groups. The esterification degree of the PGS pre-polymer was highly related to the curing temperature, time, and atmosphere. The covalent cross-linkages of PGS elastomer were relatively weak and the cross-linking density of the polymer chains was not sufficient. The presence of nanoparticles as fillers in the cured PGS nanocomposites could hinder the deformation and movements of the polymer chains. The GnPs with a plane shape also greatly inhibited the free deformation of the polymer.

Those existing metallic carboxylates confirmed the reaction of metallic nanoparticles and PGS pre-polymer during PGS nanocomposites synthesis.

$$2\,(\text{–COOH}) + \text{MgO} \rightarrow (\text{–COO}^{-})_2\,\text{Mg}^{2+} + \text{H}_2\text{O} \qquad \text{Eq. (3)}$$

$$2\,(\text{–COOH}) + \text{Mg}^{2+}(\text{OH}^{-})_2 \rightarrow (\text{–COO}^{-})_2\,\text{Mg}^{2+} + 2\text{H}_2\text{O} \qquad \text{Eq. (4)}$$

Secondly, the formation of metal carboxylate also contributed to the crosslinking of PGS composites. During the curing process, the esterification of PGS pre-polymer

generated H_2O as a reaction product, which facilitates hydrolysis of nanoparticles and release of metallic ions. The carboxylic acid groups of PGS pre-polymer and the metallic ions of nanoparticles formed ionic crosslinks. These metallic ions-dicarboxylate bonding bridged different polymer chains and stiffened the network. The competition between esterification and metallic carboxylation reduced the ester bonds in the composites, compared with the pure PGS elastomer. As shown in Fig. 1.5, the glass transition region on the DSC curve of the PGS composite becomes broader, meanwhile, the melting and recrystallization energies decreased with the nanoparticles. This showed that the crystallinity of PGS nanocomposites was reduced, as the dopants can disrupt the order of the polymer chains [51]. Also, the metal carboxylate linkages in the polymer matrix reduce the chain regularity, the concentration of ester bonds, and the extent of crystallization. Besides, compared with the TGA curve of PGS elastomer, PGS nanocomposites showed faster decomposition. As the formation of metal carboxylate linkages between dopants and the PGS chain increased the fraction of the amorphous phase in the composites [37][50] [52]. Thirdly, the graphene nameplates may generate solvent cross-linking to the PGS polymer chains. The 1wt.% graphene content of P80M19G1 samples has enhanced Young's modulus and ultimate tensile strength over P80M20 samples, with 1.24 and 1.38 folds.

The dopants affect the hydrophilicity and swelling properties of pristine PGS greatly. The nanoparticle dopants greatly decreased the sol contents of PGS nanocomposites, compared with the pure PGS elastomer. As shown in Fig. 1.6, the PGS elastomer with high sol content absorbed more THF solution and yielded larger expansions.

This can be attributed to the structure change and cross-linking density increase by reaction with nanoparticles. The strong ionic group in the polymer backbone of composites can help to resist swelling in the relatively non-polar THF solvent [35]. PGS showed different swelling behavior in different organic solvents. The swelling behavior in water is smaller.

1.4.2. The Impact on Electrical Properties

The interaction between nanoparticles and matrix is important to characterize the effect on electrical properties. The interface effect is a result of the interfacial charge carrier tunneling, enhancing the interfacial conductivity, which depends on the filler percentage. When the filler percentage increases, the average distance between fillers decreases, causing the extra charge carriers to move across the interface between the GnPs and the matrix.

As MgO and ZnO NPs were ceramic phases that were not conducive. The GnPs dopants improved the electrical conductivity greatly. From another researcher, 1 wt.% GnPs is still far below the percolation threshold [38, 39]. In Bode diagrams Fig. 1.8(d), their variations of the electrical resistivity with the frequency for all PGS nanocomposites. In the low-frequency region, a plateau is observed, in the regions of high frequencies, there is a decrease in the resistivity when frequency increase. Similar results were observed in other researcher studies [39].

The promising potential for application as cardiac repair patch material, for example, is clear from a comparison with the electrical conductivity of myocardial tissue

(1.6×10^{-3} S/cm (longitudinally) and 5×10^{-5} S/cm (transversally) [37]. The current results could be further improved to meet the application requirement.

1.4.3. Influence of Compositions and Surface Pattern on Behaviors of BMSCs

Comparing the cell adhesion density of control groups, The PGS elastomer possesses good cytocompatibility with BMSCs. The BMSCs of direct contact and indirect contact with PGS elastomer show normal morphology, shape, and spreading area. From the control groups, the increasing nanoparticles (MgO NPs and ZnO NPs) exhibited negative impacts on BMSCs adherence, as shown in Fig. 1.9. This result matches with previous works [20]. The degradation products of MgO and ZnO NPs led to a statistically significant increase in pH values, compared with BMSCs only control. The pH increase could be a factor contributing to the BMSCs reduction. This indicated that the effects of MgO NPs and ZnO NPs on BMSCs adhesion density and viability are dose-dependent.

For many biomedical applications, such as regenerative medicine, tissue regeneration, and repair, vascular graft implantation, etc, cells are typically seeded on the surface of scaffolds before implantation and benefit from the capacity to manipulate cell shape and build tissues with finely controlled morphology [40]. Cellular alignment is important for a variety of biological processes, including cell-cell and cell-matrix interactions. Our results showed that BMSCs on the substrate preferred to align along the grooves and exhibited increased body aspect ratios. Other research found similar behaviors for endothelial cells on polydimethylsiloxane (PDMS) substrates [41] [42]. The study demonstrated that surface microgroove of substrates enhances BMSCs response compared

with non-patterned control surfaces. Elongated BMSCs morphology along the groove has been observed. The formation of focal contacts along the grooved patterns triggered BMSCs morphological response that increased with decreasing groove width and increasing groove aspect ratio. Cipriano et.al reported [43] the alignment of BMSCs on Titanium with different pattern sizes from 0.5 to 50 μm. Studies evaluating BMSCs morphological responses to grooved patterns in 72 and 120 hours cultures on PLA showed that focal contacts formed preferentially and elongated parallel to the grating axis of 1 μm and 2 μm-wide grooves compared to 5 μm and 10 μm-wide grooves, and smooth surfaces [44]. The BMSCs alignment and morphological response observed in the current study on patterned PGS elastomer and composites are in agreement with the response of endothelial cells to similar substrates.

1.5. CONCLUSION

In this work, triphasic elastomeric PGS nanocomposite was processed by mixing the nanofiller (MgO NPs, ZnO NPs, GnPs) with PGS pre-polymer and curing the samples at 120 °C. The PGS nanocomposites have demonstrated enhanced cross-linking density due to the formation of metal carboxylate linkages, which contributed to an increase in tensile modulus of elasticity, and reduction of swelling. Furthermore, the electrochemical impedance spectroscopy (EIS) results indicate that GnPs have great reductions in impedance. The mechanical, electrical properties, and cytocompatibility properties of triphasic PGS nanocomposite are influenced by the amount of filler. These enhanced mechanical properties of triphasic nanocomposite make it promise in soft tissue

engineering applications such as nerve reconstruction [16], cartilage tissue [45], vascular tissue, and heart tissue [46].

Meanwhile, the BMSCs cell study result indicated that the surface patterns have shown excellent guidance of BMSCs alignment. These design and fabrication techniques of surface patterns offer a promising method for analyzing fundamental cell-substrate interaction. In addition, it showed potential approaches to modulating cell attachment, alignment, and migration in bioengineering tissue applications.

1.6 ACKNOWLEDGMENT

The authors would like to thank the University of California at Riverside for financial support the authors thank the Central Facility for Advanced Microscopy and Microanalysis (CFAMM) at the UC-Riverside for the use of SEM/EDS. The training of instruments from labmates, managers, and undergrad students.

CHAPTER 2

Electrical and Electromechanical Behavior of Graphene Nanoplatelets Doped Poly(Glycerol Sebacate) Nanocomposites

Abstract：

Conductive and piezoresistive polymeric nanocomposites have shown great potential in biomedical sensor applications. In the work, we doped conductive graphene nanoplatelets (GnPs) into poly(glycerol sebacate) (PGS) elastomer with various GnPs contents (25 wt.%, 20 wt.%, 15 wt.%, 10 wt.%, and 5 wt.%) and cured PGS-GnPs nanocomposite films. The mechanical testing results showed that GnPs dopants enhanced the tensile strength of the PGS matrix. A percolation threshold of conducive PGS-GnPs nanocomposites was observed at approximately 10 wt.% GnPs content. The nanocomposite with 25 wt.% GnPs showed the lowest sheet resistance of 36.5 Ω. The piezoresistive behavior of PGS-GnPs nanocomposites was measured under dynamic tensile loading, the nanocomposite with 10 wt.% GnPs achieved the highest gage factor of 61.7 under 11% - 23% strain deformation. This flexible and sensitive piezoresistive sensor demonstrated excellent stability, small physical stimuli limit, and good sensitivity to detect figure bending.

Keywords: strain sensor, biodegradable, piezoresistive behavior

2.1. INTRODUCTION

Carbonaceous materials (e.g. carbon nanotube (CNT), Graphene (Gr)) have outstanding mechanical, thermal, and electrical properties, and are one of the most used fillers not only to improve the mechanical properties but also to induce electrical conductivity to insulator polymeric matrix. Many researchers have doped CNT or Gr into silicone or polymeric matrix, including (dimethylsiloxane) (PDMS), and rubbers to produce conductive polymeric composites. However, the conductive fillers are expensive. As one of the Gr derivatives, graphene nanoplatelets (GnPs) are 3−10 stacks of single-layer graphene. GnPs have unique structures and remarkable electrical conductivities but are much lower cost than CNT and Gr.

Poly(glycerol sebacate) (PGS), which is an elastomer obtained from the polycondensation of glycerol and sebacic acid, has great potential for biomedical applications due to its biodegradability and biocompatibility. Many researchers have explored the properties by incorporating PGS with PCL, PLLA, or nanoparticles to develop PGS-based composites for versatile tissue engineering applications. However, the poor electric property of PGS has limited its applications and very little research reported on the enhancement of electrical properties of PGS. Hence, it is promising to develop conductive PGS nanocomposites doped with GnPs which are compatible with large-scale and low-cost fabrication.

In this study, we demonstrate the synthesis, fabrication, and characterization of PGS-GnPs nanocomposites, especially the electrical conductivity and piezoresistivity.

Different contents of GnPs dopants (25 wt.%, 20 wt.%, 15 wt.%, 10 wt.%, and 5 wt.%) were added to the PGS pre-polymer, followed by the curing step. The effect of the concentration of the conductive dopants on morphological, thermal, physical, and chemical properties of nanocomposites was systematically assessed. Stretchable film strain sensors were fabricated and tested under dynamic tensile loading and human finger, and the results exhibited good strain-sensing characteristics.

2.2. MATERIALS AND METHODS

2.2.1. Preparation of PGS-GnPs nanocomposites

The PGS polymer was synthesized via polycondensation reactions. Briefly, equimolar glycerol and sebacate acid were mixed and heated at 120 °C under N_2 protection for 24 h, then under vacuum for another 48 h. The yielded crude pre-PGS polymer was further purified using dioxane solvent (Certified ACS, Fisher Chemical, Purity ≥ 99%) to remove the unreacted monomer residues and oligomers [47]. The purified pre-PGS polymer was dissolved in 100% ethanol (mass (mg)/volume (ml) ratio is 1:1.5). GnPs (900412, Sigma-Aldrich) of an average length of 5 μm, a thickness of 6-8 nm, and a surface area from 120-150 m^2/g) were dispersed in ethanol solution and ultrasonicated to reduce the agglomerations using a high-power sonicator (Model S-4000, Misonix).

To prepare PGS-GnPs nanocomposites, GnPs/ethanol suspension was added into pre-PGS/ethanol solution to achieve a PGS-GnPs mixture with different concentrations (25 wt.%, 20 wt.%, 15 wt.%, 10 wt.%, and 5 wt.% mass of PGS). The PGS-GnPs mixture was dispersed by ultrasonication, then degassed in a dual asymmetric centrifugal mixer (speed

mixer, FlackTek Inc). Finally, the degassed PGS-GnPs mixture was poured into Teflon molds and cured at 120 °C for 48 h under vacuum.

2.2.2. Characterization of PGS-GnPs nanocomposites,

2.2.2.1. Characterize surface morphology and wettability of PGS-GnPs Nanocomposites

The surface morphology and features of PGS elastomer and PGS-GnPs nanocomposites films were observed via optical microscopy and a field emission scanning electron microscope (SEM, Nova NanoSEM450, FEI). The 3D surface profiles were scanned and generated using 3D laser scanning microscopy (VKX150, Keyence). The microstructure of the PGS elastomer and PGS-GnPs nanocomposites on the surface and cross-section was observed under SEM. The surface wettability was evaluated by water contact angles measured via a goniometer (type G16, Wet scientific).

2.2.2.2. Analyze Cystallinity and Chemical Bondings of PGS-GnPs Nanocomposites

The attenuated total reflectance-Fourier transform infrared (FTIR-ATR) spectroscopy (Thermo Scientific™ Nicolet™ iS10) was collected and analyzed using OMNIC software. The FTIR-ATR spectra were measured in the wavenumber range of 400-4000 cm^{-1}. 2.3 Analyze thermal properties. The crystalline phase structure of PGS elastomer and PGS-GnPs nanocomposites were determined by X-ray diffraction spectroscopy (XRD, PANalytical Empyrean Series 2) measurements. Data were collected over the range $2\theta = 2° – 60°$ using a step size of 0.02° at a speed of 0.25° min^{-1}. These measurements allowed studying the homogeneity of the distribution of inorganic particles and exploring the metallic and organic bonds between PGS and nanoparticles.

2.2.2.3. Characterize Mechanical, Electrical, and Electromechanical Property of PGS-GnPs Nanocomposites

The mechanical properties of PGS elastomer and PGS-GnPs nanocomposites were measured through the tensile test of an Instron 5969 Dual Column Testing System, following the ASTM D3039 standard test method. The tensile test was conducted with a 500 N load cell at a constant displacement rate of 2 mm/min. The samples were proportionally cut into strips with sizes scaled down to 20 mm × 5 mm × 0.1 mm, according to the ASTM D3039 standard. All samples were elongated to failure. Tensile modulus of elasticity (*E*) and ultimate tensile strength (*UTS*) at break was extracted and plotted.

The electrical properties of PGS- GnPs nanocomposites and elastomer were quantified by sheet resistance (R_o, ohms per square, Ω). Briefly, two equal-sized electrodes are placed in good contact on two ends of square samples. The distance between electrodes is equal to the width of the electrode by 1 cm. Two conductive copper tapes were bonded on the ends of electrodes and connected to a digital multimeter (KEITHLEY 2100 6 1/2 Digital Multimeter) under static conditions. In addition, the piezoresistive behavior of PGS-GnPs nanocomposites was measured by clamping the samples onto a tensile test instrument and recording the resistance change in real time during stretching until it ruptured. The GF, which is a ratio of relative sheet resistance change ($\Delta R/R_o$, R_o is the initial sheet resistance and ΔR is the sheet resistance change at various strain levels) and strain change, were analyzed to evaluate the sensor sensitivity. Further, the GF was measured under cyclic loading repeatedly to test the stability.

2.2.2.4. Investigate Cytocompatibility of PGS-GnPs Nanocomposites in BMSCs Culture

To explore the potential applications of PGS-GnPs nanocomposites as implanted sensors inside the human body, the compatibility with BMSCs were analyzed. Rat BMSCs were extracted from the femur and tibia of juvenile Sprague Dawley rats according to the established protocol approved by the Institutional Animal Care and Use Committee (IACUC) at the University of California at Riverside. BMSCs were cultured in fresh DMEM in a T-75 flask under standard cell culture conditions (37 °C, 5 wt.% CO_2/95 wt.% air, humidified environment) in a cell culture incubator (MCO-19AIC, Sanyo Scientific). Before cell seeding, the PGS elastomer and PGS-GnPs nanocomposites were soaked in ethanol and DMEM to remove the unreacted monomers. BMSCs were seeded at a density of 10,000 cells/cm^2 in 3 mL DMEM into each well of a 12-well tissue culture-treated plate (Corning, Falcon, 353043).

After 24 h cell culture, the 3 mL DMEMs media was collected for post-culture analysis, and the non-adherent BMSCs were washed away using phosphate-buffered saline (PBS). The rest adherent BMSCs cells were fixation using 4% paraformaldehyde (Electron Microscopy Sciences, 15714-S), then stained with 4',6-Diamidino-2-Phenylindole (DAPI; Life Technologies) for the nuclei of the cells and Alexa Fluor 488-phalloidin (Life Technologies) for F-actin. The stained cells in each well were imaged using a fluorescence microscope (Nikon Eclipse Ti-S) at 10 random locations. BMSC were counted and adhesion density was calculated as the number of adhered cells per unit area.

The pH of the post-culture media was measured immediately after collection using a pre-calibrated pH meter (Symphony SB70P, VWR). The ion concentrations (Mg^{2+} and Ca^{2+}) were measured using an inductively coupled plasma optical emission spectrometry (ICP-OES; PerkinElmer Optima 8000). The Mg^{2+} and Ca^{2+} standards with ranges of 0.5–5.0 and 0.1–1.0 mg/L are from Perkin Elmer. All the experimental and control groups were run in triplicate.

2.2.3. Measurement of Electromechanical Response of Finger Motion

To demonstrate the capability of human motion detection, we have used the sample to detect the finger bending angle. Briefly, The piezoresistive strain sensor adhered to the index figure wearing a nitrile glove using adhesive copper tapes, as shown in Fig. 2.8(b). The ends of copper tapes were connected to a multimeter which provided a certain voltage (1V) and recorded the *in situ* current of the sensor when the finger kept moving. The sheet resistance (A) and relative sheet resistance ($\Delta R/R_o$) change will be extrapolated from the voltage and current.

2.2.4. Statistical Analysis

All experiments above were run in triplicate, and the data were analyzed using one-way analysis of variance (ANOVA) followed by the Tukey's honest significant difference post hoc test. The statistical analysis was performed using GraphPad Prism 8.4.3 software. A statistically significant difference was considered at $p < 0.05$.

2.3. RESULTS

2.3.1. Surface Topography and Microstructure of PGS-GnPs Nanocomposites

The top surface and cross-section morphology and microstructure characterization of PGS-GnPs nanocomposite and pristine PGS elastomer samples are shown in Fig. 2.1. The PGS elastomers show a very flat and intact top surface Fig. 2.1(f1) and cross-section Fig. 2.1(f2) without any features. As a comparison, PGS-GnPs nanocomposites exhibited uniform GnPs distributions on the top surface of samples, shown in Fig. 2.1(a1-e1). On the surface of the 5 wt.% PGS-GnPs sample, GnPs are isolated protuberances with different orientations and separated from each other. As the GnPs content (10 wt.% and 15 wt.% of GnPs) increases, nanocomposites show interlaced wavy shapes on the surface. For nanocomposites with 20 wt.%, and 25 wt.% GnPs, GnPs are physically in contact and stacked with small pores around the boundary. Fig. 2.1(a2-e2) shows the cross-section characterization of PGS-GnPs nanocomposites which exhibited laminar graphene nanoplatelet structures. Interconnected slim cavities ranging from 4 μm to 30 μm and small pores (< 3 μm) were observed between the graphene nanoplatelets. Compared with PGS-GnPs nanocomposites of lower GnPs contents, the ones of higher GnPs contents possess more pores and wider and longer cavities.

Fig. 2.1(a3-f3) shows the top surface morphology of PGS-GnPs nanocomposites observed via laser scanning microscopy at a magnification of 480x. The PGS elastomer (Fig. 2.1(f3)) has a clean and flat surface, while PGS-GnPs nanocomposites exhibited black substrate with stacked GnPs which have flake-like shapes. The roughness average (R_a) of

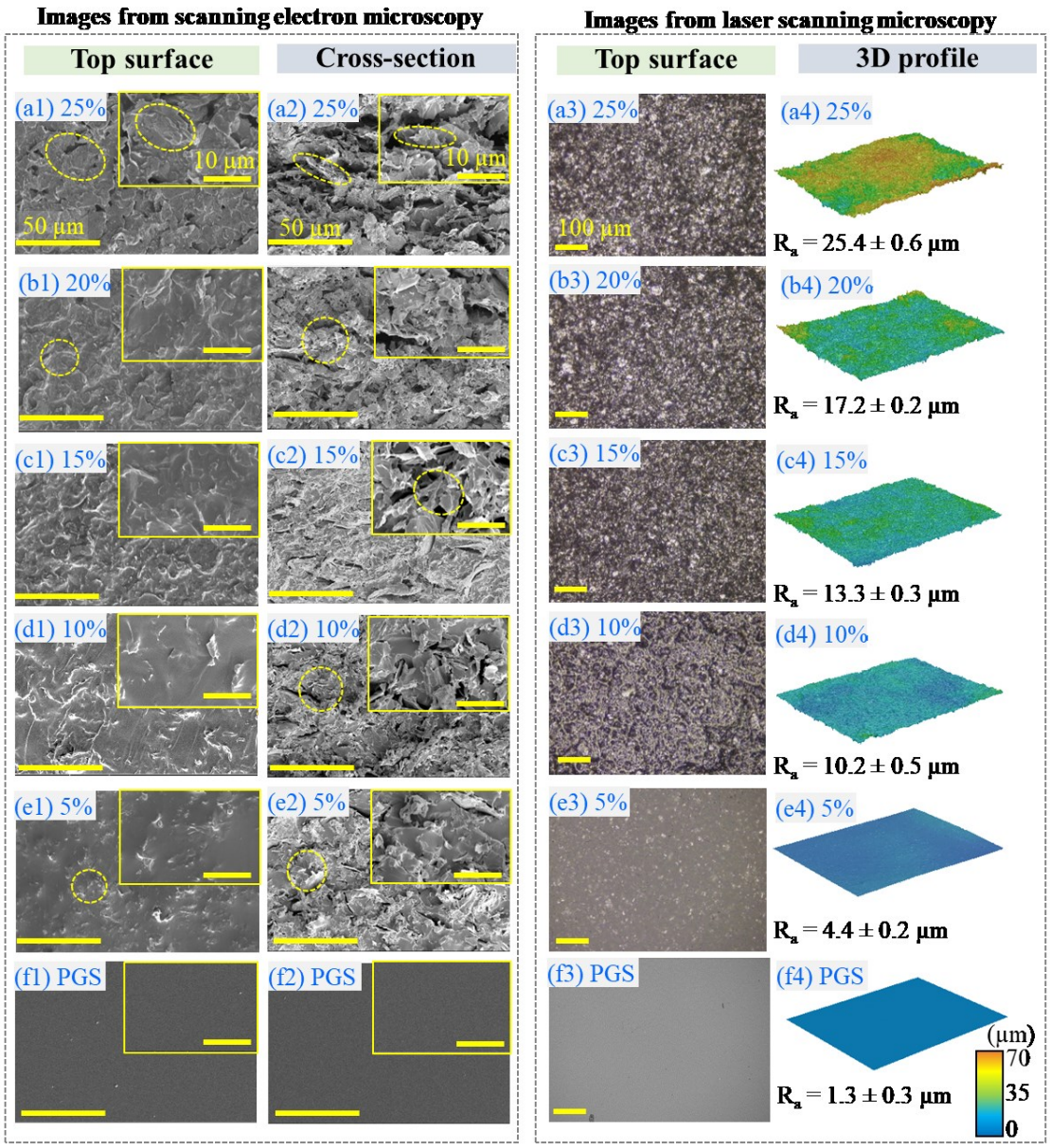

Fig. 2.1. Characterization of surface and microstructure of PGS-GnPs nanocomposites and PGS elastomer. (a1)-(f1) and (a2)-(f2) are SEM images representing the top surface and cross-sections at 1000× magnification for nanocomposites with 25 wt%, 20 wt%, 15 wt%, 10 wt% and 5 wt% of GnPs, and PGS elastomer, respectively. The yellow dash circles indicate the GnPs nanostructure in the elastomer matrix. The inlet images are at 5000× magnification. (a3)-(f3) showed images of the top surface (area = 346000 μm^2) observed via a 3d laser microscope at 480× magnification. Their corresponding surface profiles and roughness (R_a) were scanned and exhibited in (a4)-(f4).

samples surface were evaluated 3D laser profiles (Fig. 2.1(a4-f4)) and shows an increasing trend from 1.3 ± 0.3 µm (PGS), 4.4 ± 0.2 µm (5 wt.% GnPs), 10.2 ± 0.5 µm (10 wt.% GnPs), 13.3 ± 0.3 µm (15 wt.% GnPs), 17.2 ± 0.2 µm (20 wt.% GnPs), and 25.4 ± 0.6 µm (25 wt.% GnPs).

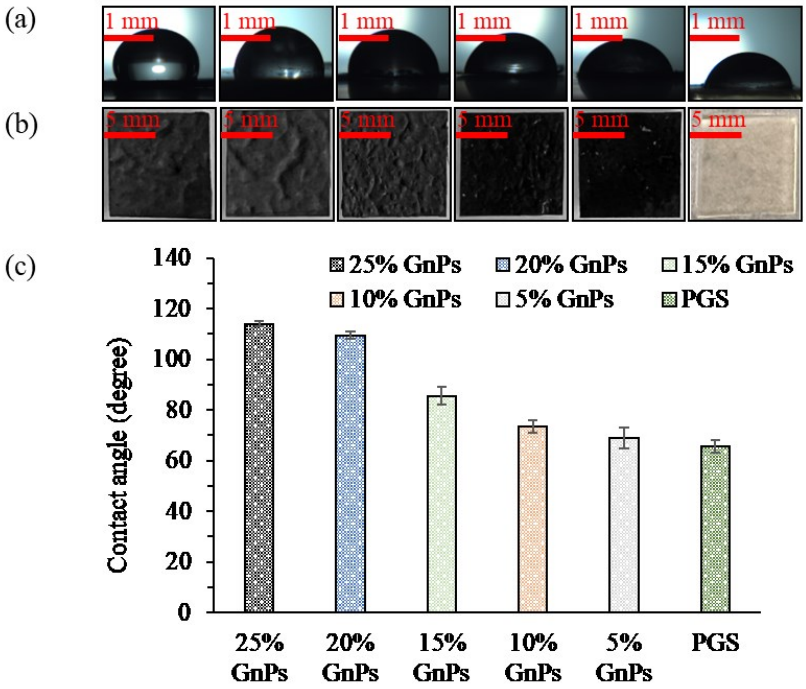

Fig. 2.2. Characterization of surface wettability of PGS-GnPs nanocomposites and PGS elastomer. Optical images in (a) and (b) respectively represent the contact angles of water droplets and top surface of samples (size of 10x10 mm square) in the order of with 25 wt%, 20 wt%, 15 wt%, 10 wt% and 5 wt% of GnPs, and PGS elastomer from left to right, (c) plots the values of measured contact angles of each sample.

The surface wettability of PGS-GnPs nanocomposites and elastomer are evaluated and compared in Fig. 2.2. The water droplets on the surface of PGS elastomer showed lower heights and larger spreading areas, compared with the water droplets on the surface of PGS-GnPs nanocomposites, as shown in Fig. 2.2(a). The contact angles of water

droplets are measured and showed increasing values from 65.6 ± 2.6° (PGS), 69 ± 4° (5 wt.% GnPs), 73.5 ± 2.5° (10 wt.% GnPs), 85.5 ± 3.5° (15 wt.% GnPs), 109.5 ± 1.5° (20 wt.% GnPs), and 114.3 ± 1.4° (25 wt.% GnPs) due to the hydrophilicity of GnPs.

2.3.2. Crystallinity, Chemical Bondings, and Cross-Linking

X-ray diffraction spectrum of PGS-GnPs nanocomposites and PGS elastomer were identified and plotted in Fig. 2.2(a). The PGS elastomer shows wide diffraction from 17° to 23.6° with a peak around $2\theta = 19.6°$, which indicates its semicrystalline structure. GnPs show a characteristic peak at $2\theta = 26.5°$ which corresponds to the d002 plane of the

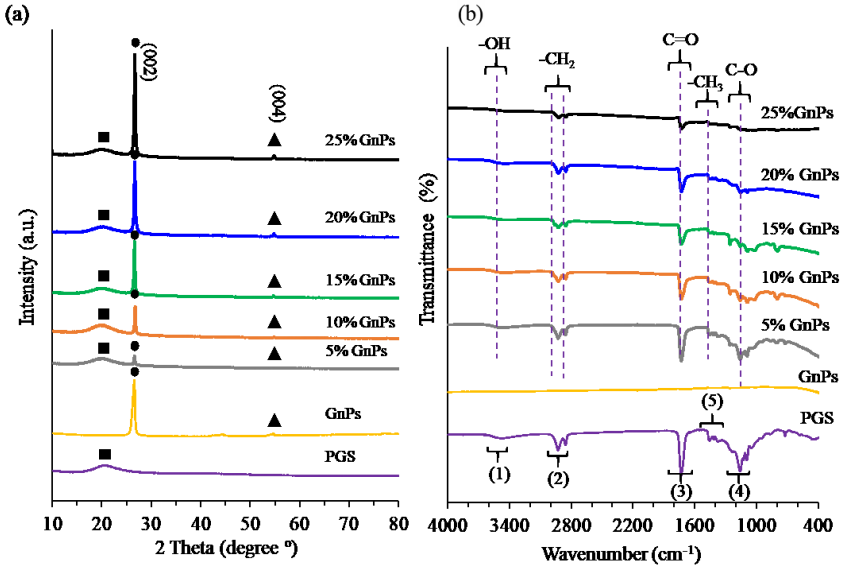

Fig. 2.3. Characterization of phase compositions and chemical bondings. (a) XRD spectrum and (b) FTIR spectrum of PGS-GnPs nanocomposites, GnPs and PGS elastomer, respectively. In XRD plots, the black dots "●" indicate the GnPs peaks at $2\theta \sim 26.5°$ which corresponds to the d002 plane, and the black triangles "▲" indicate GnPs peak at $2\theta \sim 54.6°$ (d004). The black squares "■" indicate wide diffractions of PGS from 15° to 23.6° with a peak at 2θ of 20.8°. In FTIR spectrum (b), (1) 3500-3200 cm^{-1}, hydroxyl (–OH) group; (2) 2927–2852 cm^{-1}, alkene ($–CH_2$) group; (3) and (4) at 1735 and 1159 cm^{-1} were ester group(C=O and C–O). (5) 1354–1456 cm^{-1}, methyl ($–CH_3$) bending.

exfoliated graphite nanoplatelets and another one at $2\theta =$ 54.6° (d004) of graphite. The observed XRD pattern of GnPs matches the results of previous publications [48, 49]. Same GnPs peaks were also identified on the PGS-GnPs nanocomposites with enhanced intensity as the GnPs concentrations increase from 5 wt.% to 25 wt.%.

Fig. 2.3 (b) showed the FTIR-ATR spectrum of PGS-GnPs nanocomposites and elastomers. Two primary bands were detected at 1723 cm^{-1} stretching vibration of carboxyl (C=O) and 1167 cm^{-1} stretching vibration of an ether group (C–O) in the spectrum [50]. A broad absorption peak of hydroxyl groups (-OH) at 3479 cm^{-1} and two sharp peaks at 2926 cm^{-1} and 2853 cm^{-1} indicate the stretch vibration of methyl (-CH_3) and alkane groups (-CH_2) [51]. Compared with PGS elastomer, the incorporation of GnPs results in a reduction or disappearance of the abroad hydroxyl bond (–OH, 3479 cm^{-1}) stretch and carboxyl (C=O, 1167 cm^{-1}), in contrast, the band at 1049 cm^{-1} declines which indicate an increase in the cross-linking degree [30, 52, 53].

2.3.3. Mechanical Properties of PGS Elastomer and PGS-GnPs Nanocomposites

The tensile load-extension setup and stress-strain curves of PGS-GnPs nanocomposites and elastomer are shown in Fig. 2.4(a). All samples present a linear elastic deformation up to around 172 % elongations (PGS elastomer) up to rupture. The GnPs dopants reduce the elongation values to 62.4% (5 wt.% GnPs), 25.1% (10 wt.% GnPs), 12.3% (15 wt.% GnPs), 10.4% (20 wt.% GnPs) and 5.1% (25 wt.% GnPs) strain, respectively.

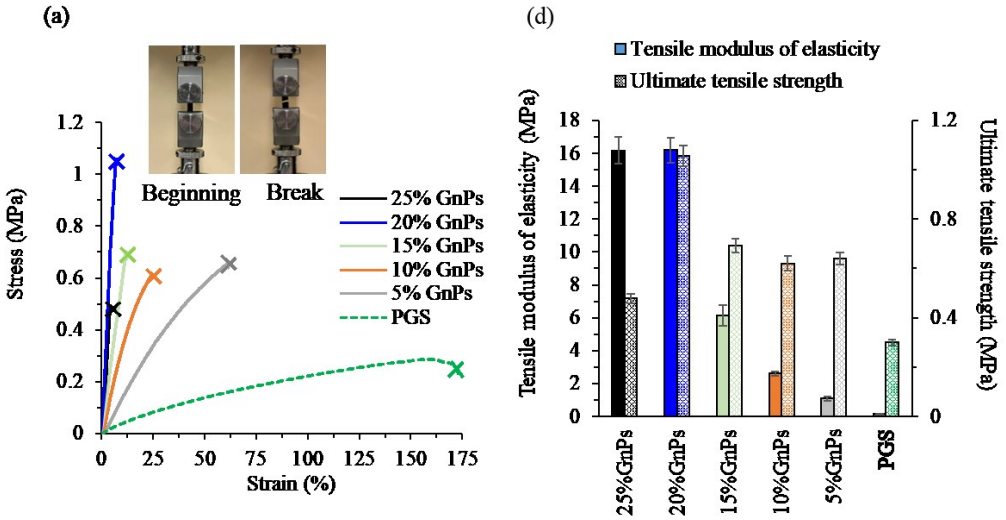

Fig. 2.4. Mechanical strength characterization of PGS-GnPs nanocomposites and PGS elastomer. (a) Stress vs. strain curves during tensile loading until rupture, and (b) plots the tensile modulus of elasticity and ultimate tensile strength of PGS-GnPs nanocomposites and PGS elastomer, respectively.

Fig. 2.4(b) plots are the tensile modulus of elasticity (*E*) and ultimate tensile strength (*UTS*) of PGS-GnPs nanocomposites and elastomer. The PGS elastomer shows *E* and *UTS* values of 1.4 ± 0.1 MPa and 0.29 ± 0.03 MPa, respectively. The incorporation of GnPs significantly improved the *E* and *UTS* values from 10.9 ± 0.1 MPa and 0.64 ± 0.03 MPa (5 wt.% GnPs), 26.2 ± 0.1 MPa and 0.63± 0.03 MPa (10 wt.% GnPs), 61.2 ± 0.1 MPa and 0.7 ± 0.03 MPa (15 wt.% GnPs), 150.8 ± 0.1 MPa and 1.1 ± 0.03 MPa (20 wt.% GnPs), 151.4 ± 0.1 MPa and 0.48 ± 0.03 MPa, (25 wt.% GnPs).

2.3.4. Electrical Resistance and Electromechanical Properties

The sheet resistance of PGS-GnPs nanocomposites and elastomer were measured under quasistatic conditions and plotted in Fig. 2.5. The GnPs dopants reduced the sheet resistance as GnPs contents increased. PGS elastomer and PGS-GnPs nanocomposite with

5 wt.% GnPs content show dielectric properties with an Rs value enormous than 106 Ω, which exceeds the limitation of the instrument. Signification reductions of sheet resistance values are observed with 10 % GnPs content, which is approximately 106117.3 Ω. This critical amount of dopant establishes a conductive network in PGS-GnPs nanocomposites, which could be regarded as a percolation threshold. Above this percolation threshold, 25 wt.% GnPs, 20 wt.% GnPs, and 15 wt.% GnPs contents yield even lower sheet resistances of 36.5 Ω, 75.8 Ω, and 582.2 Ω. The contact resistance between electrode and samples surface is negligible with usually ranges several microohms [54].

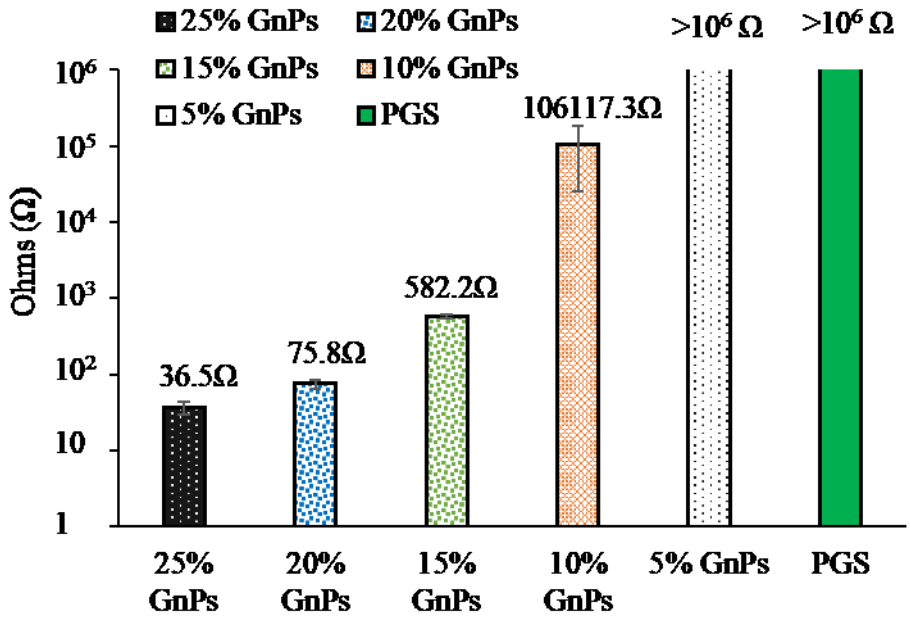

Fig. 2.5. Eelectrical sheet resistance of PGS-GnPs nanocomposites and PGS elastomer. Nanocomposite with 5 wt% GnPs and PGS elastomer show dielectric properties with a measurement exceeding the limit of the instrument.

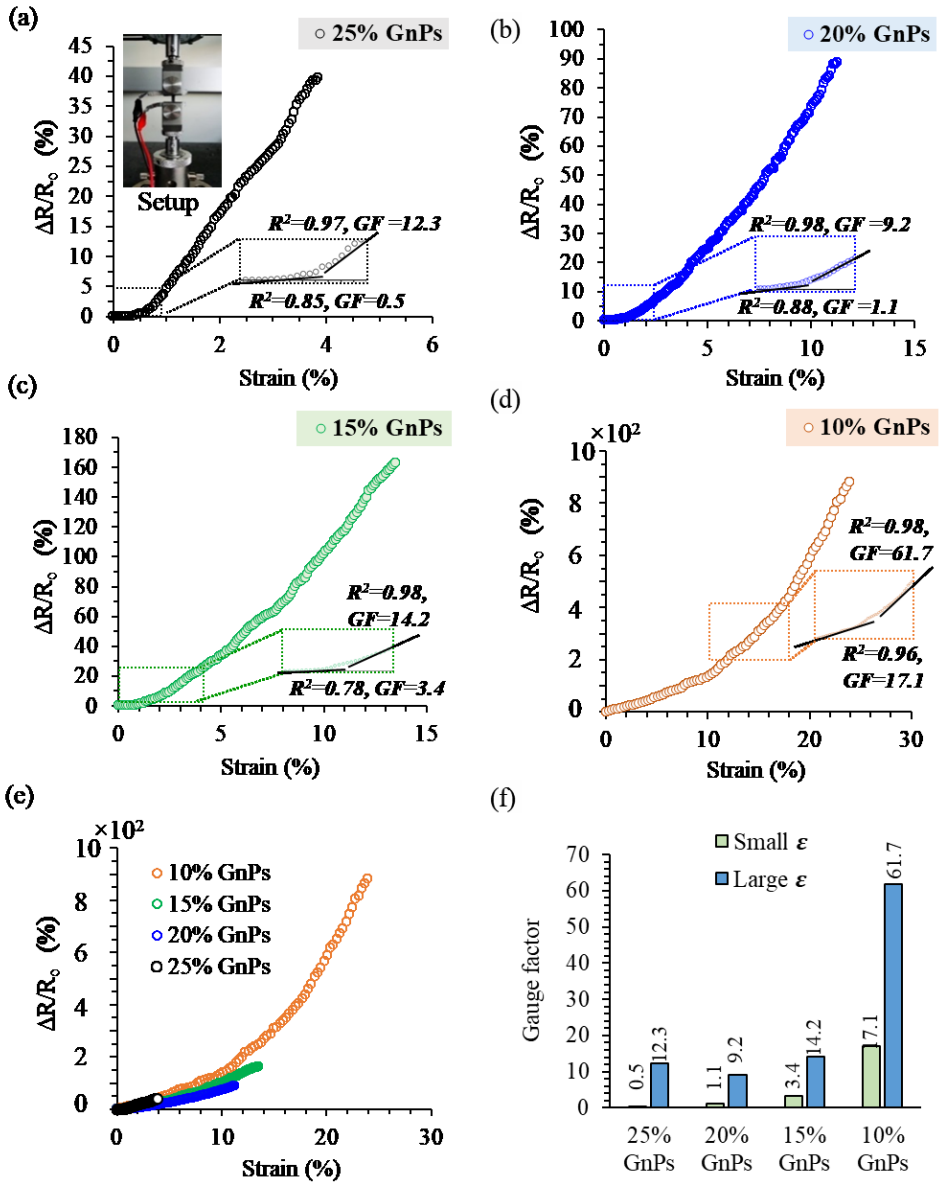

Fig. 2.6. Characterization of electromechanical properties of PGS-GnPs nanocomposites. The inlet in (a) indicates the two aluminum foil electrodes mounting on the surface of the film samples during the tensile test. (a), (b), (c) and (d) represents the relative sheet resistance variation ($\Delta R/R_o$) versus applied tensile strains for nanocomposites with 25 wt%, 20 wt%, 15 wt%, and 10 wt%, respectively. A comparison for all the above measurements

is plotted in Fig. (e). Fig. (f) shows the extrapolated GF values from the linear fitting under different strain ranges for all samples.

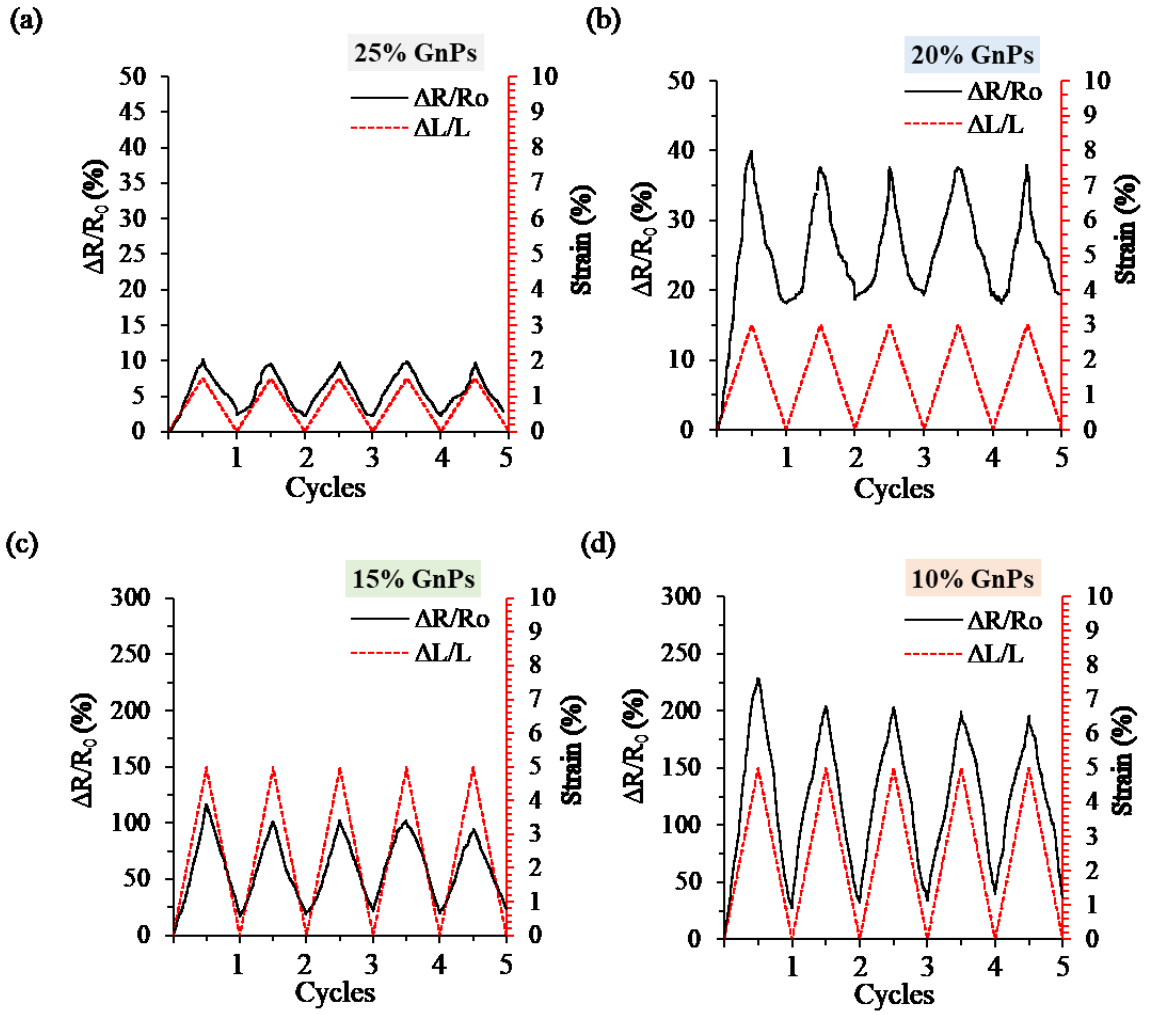

Fig. 2.7. Characterization of electrical resistance changes of the composite films under multiple cycles of mechanical loading under low strain range. (a), (b), (c) and (d) represents the relative sheet resistance variation ($\Delta R/R_o$) under 1.5%, 3%, 5% and 5% strains of samples with 25 wt%, 20 wt%, 15 wt%, and 10 wt% GnPs, respectively.

Based on the sheet resistance analysis, the PGS-GnPs nanocomposites with 25 wt.% GnPs. 20 wt.% GnPs, 15 wt.% GnPs, and 10 wt.% GnPs contents were chosen to study the

piezoresistive behavior. The change in sheet resistance ($\Delta R/R_o$) vs. strains of loading were plotted in Fig. 2.6 (a-e). The gauge factors of samples show two different values under different strain regions. Generally, the samples with lower GnPs contents possess larger elongations and higher GFs, as plotted in Fig. 2.6 (f). The GF of samples with 25 wt.% GnPs increased from 0.5 (0.8% strain) to 12.3 (4% strain), while with 20 wt.% GnPs, the GF increased from 1.1 (2.5 % strain) to 9.2 (12 % strain). The sample with 15 wt.% GnPs has GF values from 3.4 (4 % strain) to 14.2 (14 % strain) and 10 wt.% GnP show GF values from 17.1 (10 % strain) to 61.7 (24 % strain).

The repeatability of PGS-GnPs nanocomposites was studied and plotted in Fig. 2.7. The results show a repeatable and cyclic signal under different strain ranges of different GnPs contents. The PGS-GnPs nanocomposite with lower GnPs with higher strain loading exhibited larger $\Delta R/R_o$. Small hysteresis responses of $\Delta R/R_o$ were observed during cyclic loading. This could be owed to the initial breakage of GnPs contacts, leading to a slight increase of electrical resistance.

2.3.5. BMSCs Morphology, Adhesion Density, and Post-Culture Media Analyses

The BMSCs adherence, distribution, and morphology were studied after actin staining. The fluorescence microscope images (Fig. 2.8) indicate that the BMSCs are attached to the sample's surface and the well surface surrounding the samples. The BMSCs adhered to the surface of the PGS elastomer and the surrounding well surface appeared normal and spreading, though the slightly lower amount of BMSCs compared with the

amount of Glass and BMSCs control group. In the contrast, the BMSCs surrounding the surface of PGS-GnPs nanocomposites appeared much smaller spreading areas and

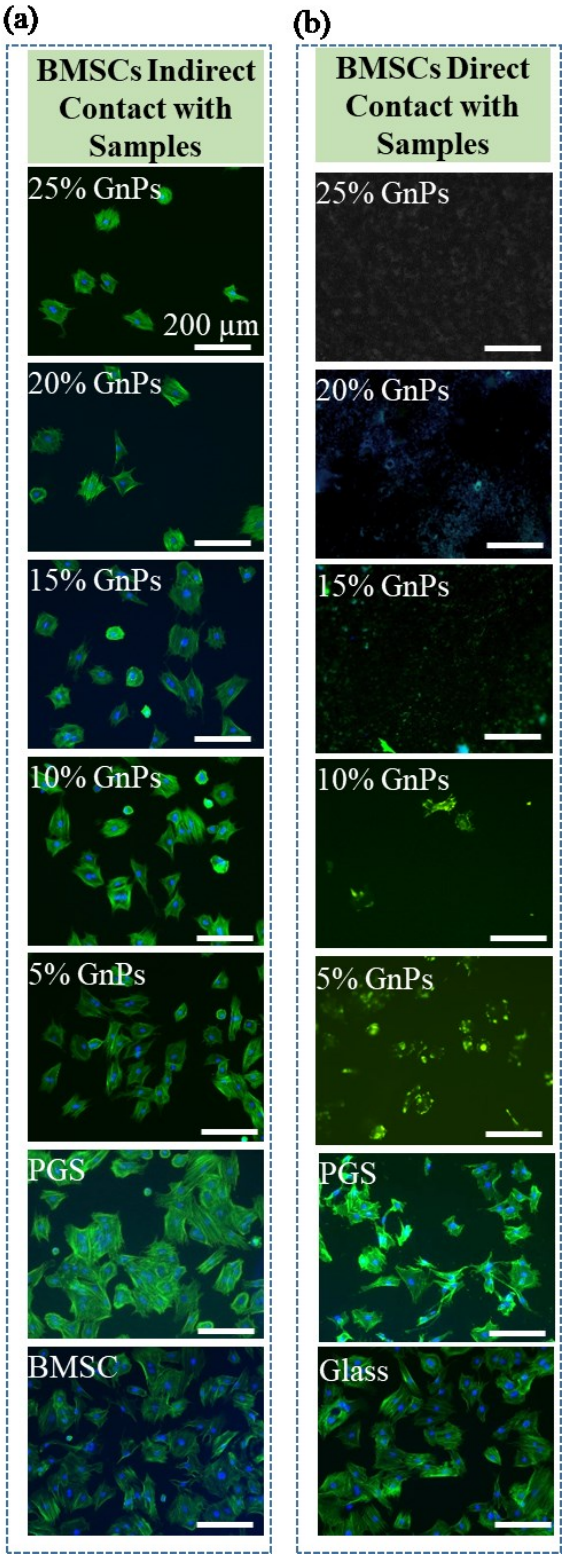

Fig. 2.8. Cell cytocompatibility analysis of BMSCs and PGS-GnPs nanocomposites and PGS elastomer. (a) and (b) indicated the fluorescence images of BMSC adhesion and morphology on the surfaces of samples and controls (direct contact) and on the surface of well plate surrounding the samples and controls (indirect contact) after in vitro culture for 24 h. The original magnification is 100x, The scale bar is 200 µm. F-actin of BMSCs was stained with Alexa Fluor 488 phalloidin as indicated in green color. BMSCs nucleus was stained with DAPI as indicated in blue color.

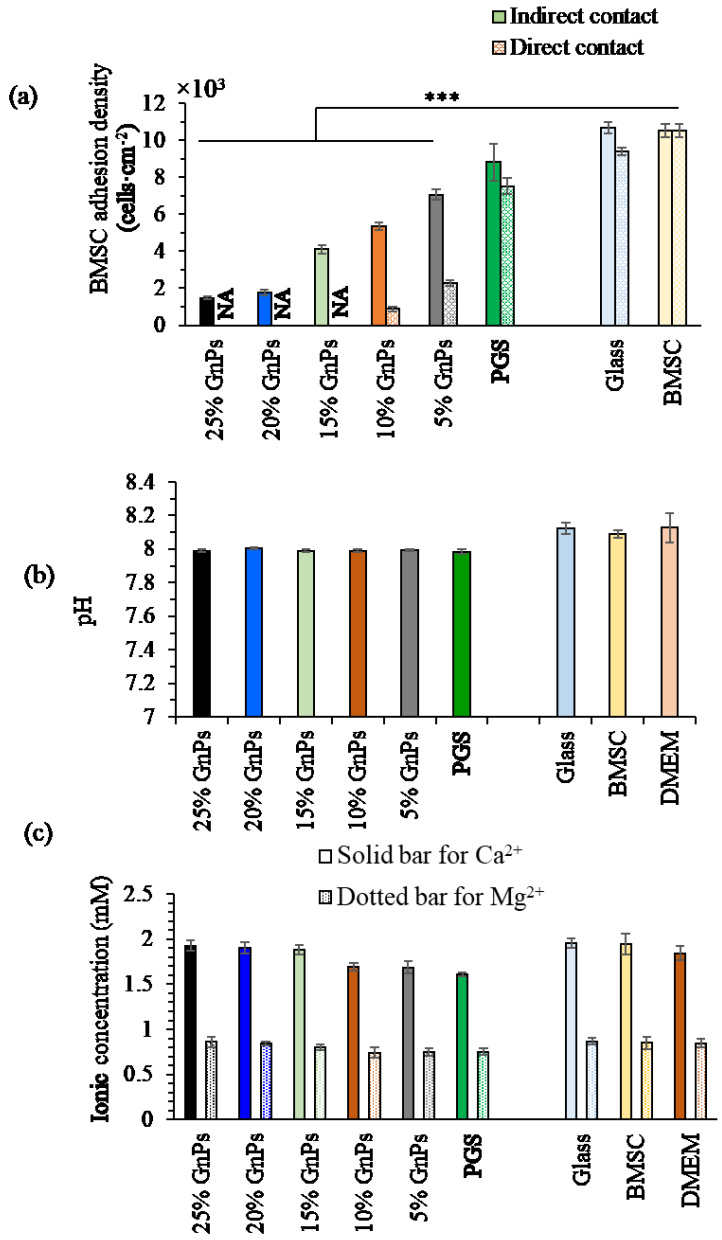

Fig. 2.9. Quantitative analyses of adhesion of BMSCs and postculture media analysis. (a) adhesion density of BMSCs under indirect contact and direct contact conditions. (b) pH and (c) Ca^{2+} ion and Mg^{2+} ion concentrations and in the media after 24-h direct culture of BMSCs with the samples and controls. The values of pH and ion concentrations were the average of media of triple wells. *$p < 0.05$, **$p < 0.01$, ***$p < 0.001$ when compared with the BMSC control.

polygonal shapes. BMSCs on the surface of PGS-GnPs nanocomposites with 5 wt.% GnPs contents showed unhealthy and abnormal shape, while much less BMSCs adherence was observed on PGS-GnPs nanocomposites with higher GnPs contents (25 wt.%, 20 wt.%, 15 wt.%, and 10 wt.%).

The quantitative assessment of BMSCs adhesion density after 24 h under direct and indirect contact with the tested samples was calculated and depicted in Fig. 2.9(a). For direct contact with samples, the adhesion density of BMSCs on the surface of the PGS elastomer is slightly lower than the value of the control groups. However, the adhesion density of BMSCs on the surface of PGS-GnPs nanocomposites was significantly reduced. Specifically, the PGS-GnPs nanocomposites with 25 wt.% and 20 wt.%, GnPs contents present cell density of zero. For the indirect contact with samples, PGS elastomer samples have slightly lower BMSCs cell density compared with control groups. PGS-GnPs nanocomposite samples show decreasing cell density as the GnPs contents increase.

Fig. 2.9(b) and (c) show the pH and ion concentration of the media collected after 24 h of culture with BMSCs. PGS-GnPs nanocomposites and PGS elastomer samples showed slightly lower pH values than that of the control groups. No statistically significant difference was not detected among the PGS-GnPs nanocomposites and PGS elastomer samples. The Ca^{2+} and Mg^{2+} ion concentrations in the media, PGS-GnPs nanocomposites, and PGS elastomer show lower values than those of the control group. PGS-GnPs nanocomposite with higher GnPs contents (25 wt.%, 20 wt.%, and 15 wt.%) have higher values than those of lower GnPs contents (10 wt.% and 5 wt.%), and PGS elastomer.

2.3.6. Electromechanical Response of Finger Motion

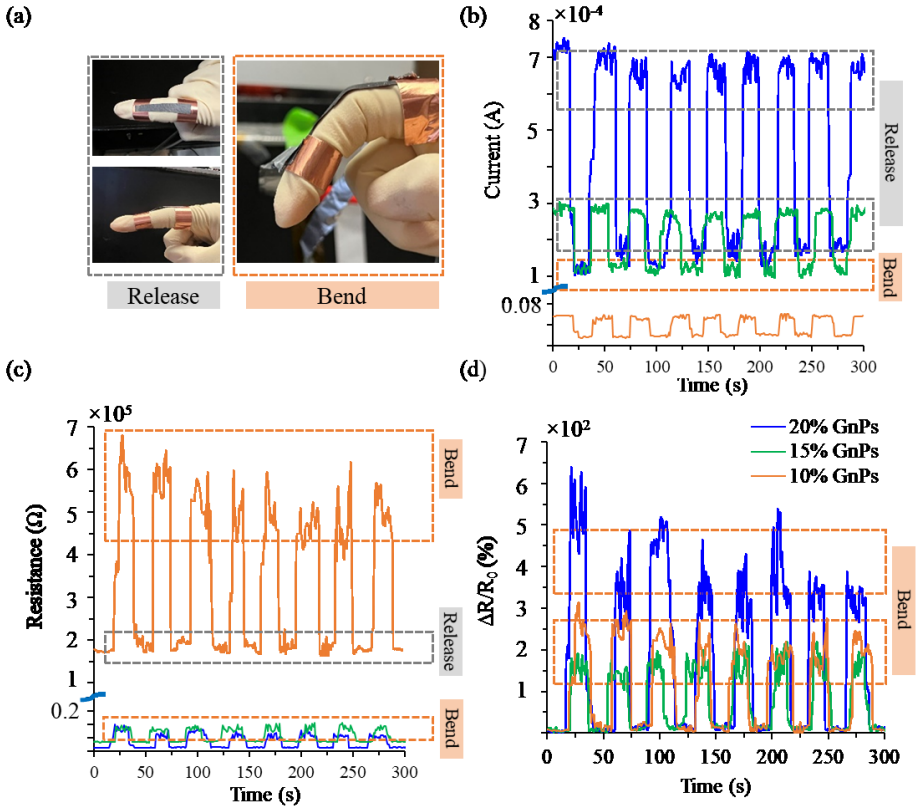

Fig. 2.10. Measurement of electromechanical responses of film sensors during finger bending detections. (a) Photographs showing the PGS-GnPs film sensors adhered to the back of a finger. (b), (c) and (d) indicated the relative resistance variation ($\Delta R/R_o$) , current (A), and resistance (Ω) in finger motion from bending to release of samples with 20 wt%, 15 wt%, and 10 wt% GnPs. The measurements were recorded for 9 repeated cycles under constant voltage of 1V.

To demonstrate the potential of PGS-GnPs nanocomposite films in wearable applications, we chose PGS-GnPs nanocomposites with 20 wt.%, 15 wt.%, and 10 wt.% GnPs contents to fabricate stretchable motion sensors for small movements. Fig. 2.10(a) shows a film sensor mounted on the index finger. The measured current (A), sheet resistance (Ω) and relative sheet resistance ($\Delta R/R_o$) change have significantly varied during finger motion from release to bend, as shown in Fig. 2.10(b-d). The sample with 20 wt.%

GnPs exhibited the largest relative sheet resistance changes than that of the sample with 15 wt.% and 10 wt.% GnPs. During these eight cycles, the signals showed great consistency. Under 1(V) power supply, the sample with 25 wt.% GnPs show a current around 6.8×10^{-4} (Amp) under release and increases sharply to 1.4×10^{-4} (Amp) under bending status, the sample with 20 wt.% GnPs exhibited smaller current values of 3.1×10^{-4} (Amp) under release and 1.1×10^{-4} (Amp) under bending status, the sample with 15 wt.% GnPs has the lowest current among them, which is approximately 0.07×10^{-4} (Amp) under release and 0.02×10^{-4} (Amp) under bending status. The value of sheet resistance change ($\Delta R/R_o$) increased under bending status and returned to the initial values when the finger was released.

2.4. DISCUSSION

2.4.1. Effect of GnPs dopants on surface morphology, interface, and mechanical properties of PGS-GnPs nanocomposites

The enhancement of the mechanical properties of PGS-GnPs nanocomposite relies on many factors, such as good dispersion of GnPs, interfacial adhesion between phases, and morphology of nanocomposite. The GnPs filler is very uniformly dispersed in the PGS matrix. With high GnPs contents (15 wt.%, 20 wt.%, and 25 wt.%), the GnPs forms interconnected network and agglomerates in PGS. Similar appearances were also found in poly(lactic acid) (PLA) and GnPs nanocomposite [48, 55, 56]. The mechanical properties of PGS-GnPs nanocomposites showed monotonously enhancements for both ultimate tensile strength and tensile modulus of elasticity from 5 wt.% to 20 wt.% of GnPs contents.

Simiar performance were also observed in other GnPs nanocomposites, such as rubbuer [57]. However, 25 wt.% of GnPs will yield a rigid behavior as overfull dopants inhibited the cross linking of the PGS matrices.

The presence of GnPs on the surface greatly affects the wettability of samples and increases the hydrophobic effects, which were observed in others' reports [58, 59]. From the XRD spectrum Fig. 3(a), there is no shift with GnPs' peak, which indicates that GnPs maintained intact platelets spacing and structure in the matrix. The wide peaks of PGS didn't change which shows that GnPs dopants didn't affect the crystallinity of the PGS matrix. Higher GnPs content in PGS-GnPs nanocomposites possess higher crystallinity degrees, which results in higher tensile modulus of elasticity but lower elongations to rupture. With 25 wt.% and 20 wt.% of GnPs, the nanocomposite become brittle due to the rigid amorphous phase and a higher fraction of trans-planar mesophase [60]. This typical mechanical behavior for brittle thermosetting polymer matches with CNT-vinyl ester composites [61], etc.

2.4.2. Influence of GnPs dopants on electrical and electromechanical behavior of PGS-GnPs nanocomposites

GnPs have demonstrated great capability as dopants to enhance the electrical conductivity of PGS elastomer. A pertinent theory to describe the electrical behavior of doped polymeric nanocomposites is the percolation threshold, which states the presence of interconnected GnPs network results in a dramatically enhanced electrical conductivity [55]. The reduction of sheet resistance of PGS nanocomposites could be attributed to two

major reasons. Firstly, the interconnected GnPs (as shown in Fig. 2.1) could generate conductive routes and leakage current, and secondly, the small pores and cavities between GnPs could form electron tunnels to transmit electrons and transfer tunneling current [62]. The PGS-GnPs nanocomposite with 5 wt.% GnPs show separated GnPs without sufficient interconnections, as shown in Fig. 2.1(e1), thus it possesses dielectric properties. Samples with higher GnPs contents (25 wt.%, 20 wt.%, 15 wt.%, and 10 wt.%) observe greatly increased contact between GnPs (as shown in Fig. 2.1) and exhibited a significant reduction of sheet resistance.

The percolation threshold of 10 wt.% GnPs is close to others' work, such as 7-8 wt.% for PLA-GnP composites [48], 8-10 wt.% for Poly(propylene)-GnPs nanocomposites [49], 10 wt.% for CNT-polycarbonate nanocomposites [60], etc. was well established around 20 wt.% GnPs. In addition, when GnPs content increase from 20 wt.% to 25 wt.%, the sheet resistance slightly decreases from 75.8 Ω to 36.5 Ω, which indicates the cross-linked network structure of the conductive GnPs. The sheet resistance of the PGS-GnPs nanocomposites is also varying during tensile loading deformations because of the changes in their inner conductive networks of GnPs and tunneling resistances between GnPs. When electrical routes form at the percolation threshold, the sheet resistance reduces dramatically. If the film is stretched, the conductive route breaks down and results in increased surface resistance.

The GF extrapolated from the electromechanical test is a key parameter to evaluate the sensitivity to strain change. The relatively higher GF values upon further stretching arises could be owing to more severe separations between GnPs at higher strain loading

[63]. Our PGS-GnPs nanocomposites exhibit much larger GF, compared with other reports. Kong et.al observed GFs of PDMS-carbon-black composites with a value from 2-10 [64]. Wong et. al found PDMS-graphene composites with GFs values of 3.9–233 [65]. For the nanocomposites with 10 wt.% of GnPs, the sample exhibited high and stable GF value of 61.7 under stain ranges from 12 % to 24 %, which is much higher elongation than graphene nanopaper (maximum 6% strain) [63]. The GF values are much higher than reported film material, such as SWCNT film with GF value of up to 0.82 [66], CNT/Vinyl ester nanocomposite with GF value of 2.6 under tension [61].

From the sheet resistance change under cyclic loading conditions (Fig. 2.7), PGS-GnPs nanocomposites observed electrical hysteresis phenomena due to the viscoelastic behavior of PGS elastomer matrices. This was also found in other polymer nanocomposites such as PDMS [67]. The values of electrical hysteresis could be reduced by modifying the geometry of the sensors, such as wavy and zigzag shapes.

2.4.3. Potential Applications for Piezoresistive and Capacitive Sensors

The monitoring of electromechanical response during human finger motion detection using our PGS-GnPs film sensors demonstrated sharp and distinguishable signal variations. Under small strain variations of finger motion, the sample of 20 wt.% GnPs exhibited the largest signal variations from release to bending statues. Consequently, our film sensor can identify finger bending movements unambiguously. On the contrary, the sample with 10 wt.% GnPs show the largest values of GF (Fig. 2.6(d)) under high strain changes and the sample with 20 wt.% GnPs show relatively small values of GF (Fig. 2.6(b))

in the electromechanical tests. This indicates different GnPs contents would meet various favorable strain ranges. Compared with current sensors made of nondegradable silicone or conductive polymer-based materials, our PGS-GnPs film sensor showed great sensitivity and repeatability. In addition, PGS-GnPs nanocomposites possess advantages, such as easy fabrication, low cost, and good biodegradability[68], which could reduce the negative impact on the environment. Specifically, it could be used in many strain sensor applications, including human motion monitoring, blood pressure measurement, soft robots, speech recognition, electronic skin, etc.

Meanwhile, the PGS-GnPs nanocomposite with 25 wt.%, 20 wt.%, and 15 wt.% of GnPs exhibited very low sheet resistance, thus these materials showed potential to be employed as highly conductive films or layers to develop flexible and biodegradable capacitors.

2.5. CONCLUSION

In summary, our work presents a simple and reliable route to produce low-cost, environmentally friendly, and piezoresistive nanocomposites via doping GnPs into biodegradable PGS elastomer. The percentage of GnPs dopant greatly influences the mechanical, electrical, and electromechanical performance of PGS-GnPs nanocomposites. The developed sensors demonstrated superior GF values with exceptional sensitivity, repeatability, and low hysteresis. The developed piezoresistive sensors can be tailored to work in a wide range of applications with varying strain and force ranges, such as soft

wearable sensors for subtle movement (finger, wrist, face, and throat) and large joint motion (knee, wrist, and elbow).

2.6 ACKNOWLEDGMENT

The authors would like to thank the University of California at Riverside for financial support the authors thank the Central Facility for Advanced Microscopy and Microanalysis (CFAMM) at the UC-Riverside for the use of SEM. The training of instruments from labmates and managers.

CHAPTER 3

Cytocompatibility of Graphene Nanoplatelet Incorporated Poly(Glycerol Sebacate) Nanocomposites for Tissue Engineering Applications

Abstract:

Graphene family materials have shown the potential to accelerate the differentiation of stem cells into neurons. Here, we incorporated graphene nanoplatelets (GnPs) with poly(glycerol sebacate) (PGS) elastomer with various contents of GnPs (4 wt.%, 3 wt.%, 2 wt.%, 1 wt.%, 0.5 wt.%, 0.2 wt.%, and 0.1 wt.%). The GnPs dopants result in increased hydrophobicity of the PGS-GnPs nanocomposites. Meanwhile, the PGS-GnPs nanocomposites showed enhanced tensile modulus of elasticity (*E*) and ultimate tensile strength (*UTS*). The i*n vitro* cell culture with bone marrow stromal cells (BMSCs) found dose-dependent cytotoxicity of GnPs dopants. The PGS-GnPs nanocomposite with less than 1 wt.% GnPs showed good biocompatibility with BMSCs.

Keywords: PGS elastomer, GnPs dopants, mechanical properties, cytocompatibility.

3.1. INTRODUCTION

Peripheral nerve injury (PNI) is a common global clinical issue, which has significantly affected the life quality of patients and caused an enormous socioeconomic burden. PNI was mainly attributed to trauma, and less frequently, congenital defects and surgical resection secondary to tumor excision [69]. Approximately 2–5% of trauma patients have experienced a PNI and nearly 100,000 cases of peripheral nerve surgeries are performed each year in North America [70]. Although the peripheral nervous system (PNS) has a greater capability for axonal regeneration after injury than the central nervous system (CNS), spontaneous peripheral nerve repair is incomplete with poor functional recovery [71]. Thus far, various nerve repair methods have been implemented to promote nerve regeneration. For nerve injuries shorter than 5 mm, a meticulous microsurgical repair by end-to-end tensionless epineuria suturing is preferred [72]. In some cases of large nerve gaps, the interposition of grafts between the nerve stumps is required to bridge the gap and support axonal regrowth [73]. The implantation of autologous nerve grafts is the gold standard. However, it has some inherent limitations, such as the requirement of a second surgery, donor site morbidity, limited graft availability, size and geometrical mismatch, and the possibility of painful neuroma formation, etc [71, 74-76].

The desired nerve conduit should exhibit good mechanical properties, electrical conductivity, and biocompatibility to mimic the human neural tissue and stimulate cell proliferation [77]. The currently used artificial biomaterials, such as poly(glycolide) (PGA), poly(L-lactide) (PLLA), poly(dl-lactide-co-glycolide) (PLGA) [78, 79], polycaprolactone (PCL) [80], poly(lactide-ε-caprolactone) (PLA-PCL) [81], biodegradable polyurethanes

[82, 83], poly(organo) phosphazenes [84], and trimethylene carbonate–caprolactone copolymers [85] have exhibited unfavorable swelling and pro-inflammatory characteristics [16].

PGS is a synthetic, biodegradable, thermos-set and tough polymer first reported in 2002 by *Wang et al*. [14]. It exhibited nonlinear stress-strain behavior, which is typical for soft elastomer material. The elastomeric nature of PGS is due to the interaction between covalent crosslinking and a 3D network of random coils with hydroxyl groups attached to the backbone [15, 86, 87]. It has an average tensile Young's modulus in the range of 0.0250 – 1.2 MPa, the ultimate tensile strength is >0.5 MPa, and strain to failure is greater than 330 % [14-16]. The studies showed that the peripheral nerve has a strength of 11.7 MPa and a strain of 38.50 % [88, 89]. The Young modulus values are observed between 0.1 and 11.1MPa [90, 91]. For *in situ* peripheral nerve, with Young's modulus of approximately 0.45MPa [15], is a close match to that of PGS, and less stiff than other conduit materials, such as poly(L-lactide) and polyhydroxybutyrate (PHB), which has Young's modulus of 660MPa [16] and 250MPa [14], respectively. Owing to those attributes, PGS has recently been investigated for numerous potential soft tissue engineering applications such as nerve reconstruction [16], cartilage tissue [45], vascular tissue [46], and heart tissue.

Graphene (Gr), which consists of a monolayer of carbon atoms arranged in a 2D honeycomb lattice [92], and its derivatives have shown great potential in stem cell-related biomedical applications, due to the excellent flexibility, thermal properties, electrical conductivity, high strength, stiffness and biocompatibility [93, 94]. Some researchers found Gr and its derivatives reduced *in vitro* cell viability with a concentration of about 10

μg/mL [95, 96]. Akhavan et. al reported the size and dose-dependent genotoxicity of GnPs in human mesenchymal stem cells (hMSCs) [97]. Hong et. al observed that Gr-patterned substrates substantially enhanced the adhesion and neurite outgrowth of PC-12 cells [98].

Neural stem cells (NSCs) are capable to differentiate into neurons and glial cells and this process was by cell-cell and cell-extracellular matrix (ECM) interactions [99]. Since Gr had a positive interaction with differentiated neurons for electrical stimulation, its unique surface property can facilitate the differentiation of hNSCs into neurons over glia [100]. Park et. al found Gr substrate has enhanced the differentiation of human neural stem cells (hNSCs) into neurons [101, 102]. In addition, Gr and its derivatives have been used as dopants to synthesize polymer composites.

In this study, we synthesized PGS-GnPs nanocomposites with different GnPs contents. As one of the Gr derivatives, graphene nanoplatelets (GnPs) are 3−10 stacks of single-layer Gr. GnPs have unique structures and remarkable electrical conductivities but are much lower cost than Gr and carbon nanotubes. We studied the mechanical behaviors of the PGS-GnPs nanocomposites to better match the mechanical properties of nerves for artificial graft applications. Meanwhile, we systematically investigated the toxicity and biocompatibility of GnPs with bone marrow stromal cells (BMSCs) via *in vitro* cell cultures.

3.2. MATERIALS AND METHODS

3.2.1. Preparation of PGS-GnPs Nanocomposites

The PGS polymer could be synthesized via polycondensation reactions. Briefly, equimolar glycerol and sebacate acid were mixed and heated at 120 °C under N_2 protection for 24 h, then under vacuum for 48 h. The yielded crude pre-PGS polymer was further purified using dioxane solvent (Certified ACS, Fisher Chemical, Purity ≥ 99%) to remove the unreacted monomer residues and oligomers [47]. The purified pre-PGS polymer was dissolved in 100% ethanol (w/v% is 1:1.5). GnPs (900412, Sigma-Aldrich) of an average length of 5 μm, a thickness of 6-8 nm, and a surface area from 120-150 m^2/g) were dispersed in ethanol solution and ultrasonicated to reduce the agglomerations using a high-power sonicator (Model S-4000, Misonix).

To prepare PGS-GnPs nanocomposites, GnPs/ethanol suspension were added into pre-PGS/ethanol solution to achieve PGS-GnPs mixture with different mass (4 wt.%, 3 wt.%, 2 wt.%, 1 wt.%, 0.5 wt.%, 0.2 wt.%, and 0.1 wt.% of PGS). The PGS-GnPs mixture was dispersed by ultrasonication, then degassed in a dual asymmetric centrifugal mixer (speed mixer, FlackTek Inc). Finally, the degassed PGS-GnPs mixture was poured into Teflon molds and cured at 120 °C for 48 h under vacuum.

3.2.2. Characterization of PGS-GnPs Nanocomposites

3.2.2.1. Characterize Surface Properties of PGS-GnPs Nanocomposites and Elastomer

The surface morphology and microstructures of PGS-GnPs nanocomposites and PGS elastomer were investigated using an emission scanning electron microscope (SEM, Nova NanoSEM450, FEI). The surface wettability was evaluated by water contact angles

using a goniometer (type G16, Wet scientific). For each sample, a water droplet with a volume of 1 µl was dispensed on the surface of the samples.

3.2.2.2. Analyze Crystallinity and Chemical Bondings

The crystalline phase structure of PGS-GnPs nanocomposites and PGS elastomer were studied by X-ray diffraction spectroscopy (XRD, PANalytical Empyrean Series 2) measurements. Data were collected over the range $2\theta = 2° – 80°$ using a step size of 0.02° at a speed of 0.25° min^{-1}. The attenuated total reflectance-Fourier transform infrared (FTIR-ATR) spectroscopy (Thermo Scientific™ Nicolet™ iS10) was collected and analyzed using OMNIC software. The FTIR-ATR spectra were measured in the wavenumber range of 400-4000 cm^{-1}. These measurements allowed studying the homogeneity of the distribution of inorganic particles and exploring the metallic and organic bonds between PGS and nanoparticles.

3.2.2.3. Analyze Thermal Properties

The thermal properties of PGS-GnPs nanocomposites and PGS elastomer were evaluated with thermal gravimetric analysis (TGA) (Netzsch TG 209 F1 Libra) and a differential scanning calorimeter (DSC) (Netzsch DSC 214 Polyma). For TGA characterization, the PGS and PGS composites samples with a weight of approximately 3 mg were prepared and placed in alumina crucibles. A heating/cooling rate of 20 °C/min was applied from room temperature to 600 °C. For DSC analysis, we chose approximately 6 mg for each PGS-GnPs nanocomposite with different GnPs contents. The heating and

cooling rate are 20 °C/min. Multiple heating and cooling cycles are applied to ensure accuracy.

3.2.2.4. Characterize Mechanical Properties of PGS-GnPs Nanocomposites

The mechanical properties of PGS-GnPs nanocomposites and PGS elastomer were measured through the tensile test of an Instron 5969 Dual Column Testing System, following the ASTM D3039 standard test method. The tensile test was conducted with a 500 N load cell at a constant displacement rate of 2 mm/min. The samples were proportionally cut into strips with sizes scaled down to 20 mm × 5 mm × 0.1 mm, according to the ASTM D3039 standard. All samples were elongated to failure. Tensile modulus of elasticity (*E*) and ultimate tensile strength (*UTS*) at break was extracted and plotted.

3.2.2.5. Investigate Cytocompatibility of PGS-GnPs Nanocomposites in BMSCs Culture

To explore the potential applications of PGS-GnPs nanocomposite as implanted sensors inside the human body, the compatibility with BMSCs were analyzed. Rat BMSCs were extracted from the femur and tibia of juvenile Sprague Dawley rats according to the established protocol approved by the Institutional Animal Care and Use Committee (IACUC) at the University of California at Riverside. BMSCs were cultured in fresh DMEM in a T-75 flask under standard cell culture conditions (37 °C, 5% CO_2/95% air, humidified environment) in a cell culture incubator (MCO-19AIC, Sanyo Scientific). Before cell seeding, the PGS elastomer and PGS-GnPs nanocomposites were soaked in ethanol and DMEM to remove the unreacted monomers. BMSCs were seeded at a density

of 10,000 cells/cm^2 in 3 mL DMEM into each well of a 12-well tissue culture-treated plate (Corning, Falcon, 353043).

After 24 h cell culture, the 3 mL DMEMs media was collected for post-culture analysis, and the non-adherent BMSCs were washed away using phosphate-buffered saline (PBS). The rest adherent BMSCs cells were fixation using 4% paraformaldehyde (Electron Microscopy Sciences, 15714-S), then stained with 4',6-Diamidino-2-Phenylindole (DAPI; Life Technologies) for the nuclei of the cells and Alexa Fluor 488-phalloidin (Life Technologies) for F-actin. The stained cells in each well were imaged using a fluorescence microscope (Nikon Eclipse Ti-S) at 10 random locations. BMSC were counted and adhesion density was calculated as the number of adhered cells per unit area.

The pH of the post-culture media was measured immediately after collection using a pre-calibrated pH meter (Symphony SB70P, VWR). The ion concentrations (Mg^{2+} and Ca^{2+}) were measured using an inductively coupled plasma optical emission spectrometry (ICP-OES; PerkinElmer Optima 8000). The Mg^{2+} and Ca^{2+} standards with ranges of 0.5–5.0 and 0.1–1.0 mg/L are from Perkin Elmer. All the experimental and control groups were run in triplicate.

3.2.3. Statistical Analysis

All experiments above were run in triplicate, and the data were analyzed using one-way analysis of variance (ANOVA) followed by the Tukey's honest significant difference post hoc test. The statistical analysis was performed using GraphPad Prism 8.4.3 software. Statistically, a significant difference was considered at $p < 0.05$.

3.3. RESULTS

3.3.1. Surface Topography and Microstructure of PGS-GnPs Nanocomposites

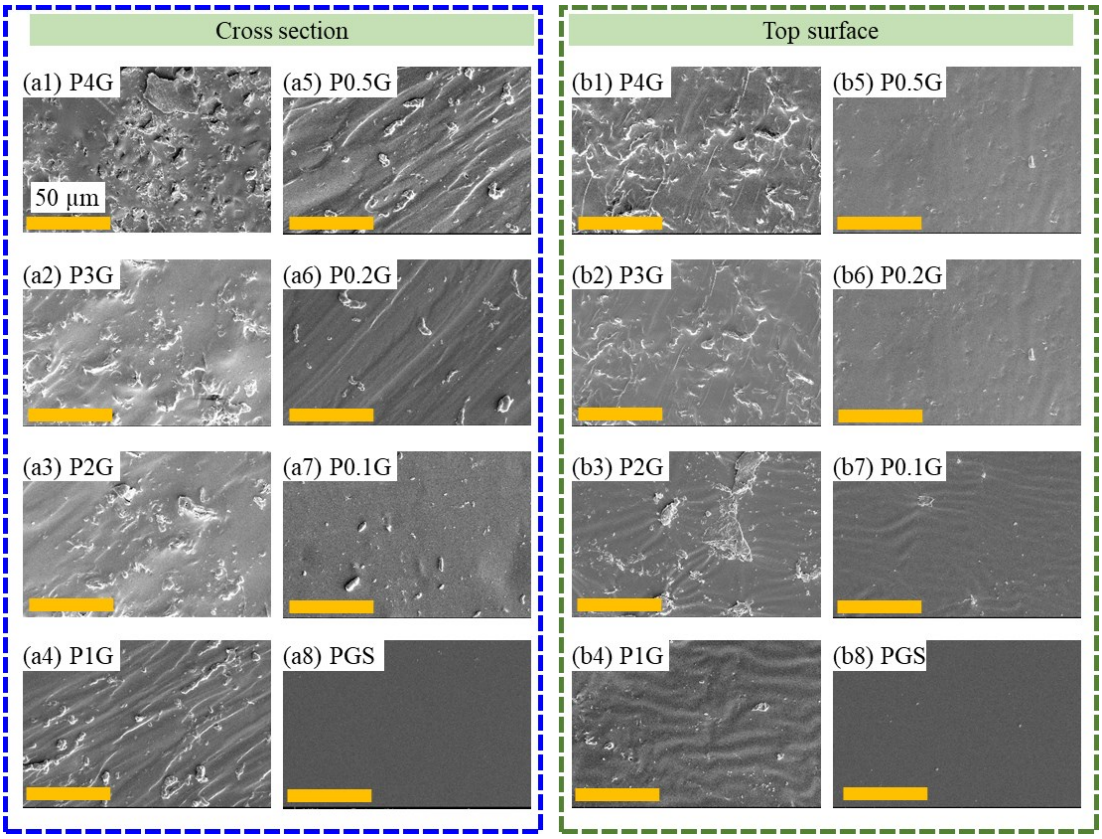

Fig. 3.1. Cross-section and surface morphology of the PGS elastomer and nanocomposites. SEM images (a1)-(a8) show the cross-section feature of P4G. P3G, P2G, P1G, P0.5G, P0.2G, P0.1G, and PGS at original 10,000x magnification, respectively. (b1)-(b2) indicates the top surface morphology of PGS-GnPs nanocomposite and elastomer.

The surface morphology and topography of the PGS-GnPs nanocomposite specimen were observed using scanning electron microscopy (SEM), as shown in Fig. 2.1. The cross-section and top surface of the PGS elastomer show a clean and flat appearance, as shown in Fig. 2.1(a8) and (b8), respectively. The cross-section of PGS-GnPs nanocomposites with 4 wt.% GnPs shows uniformly distributed clusters of GnPs, while

nanocomposites with 3 wt.%, 2 wt.%, 1 wt.% and 0.5 wt.% of GnPs separated GnPs features. The cross-section of samples with 0.2 wt.%, and 0.1 wt.% of GnPs found a few random GnPs debris, Fig. 2.1(a7) and (a8). From the top surface images of samples with 4 wt.% and 3 wt.% of GnPs, interconnect GnPs protuberances with wavy shape were observed dispersion uniformly, while samples with 2 wt.% of GnPs showed a few separated GnPs clusters. No GnPs features were observed on the surface of samples of less than 1 wt.% GnPs contents.

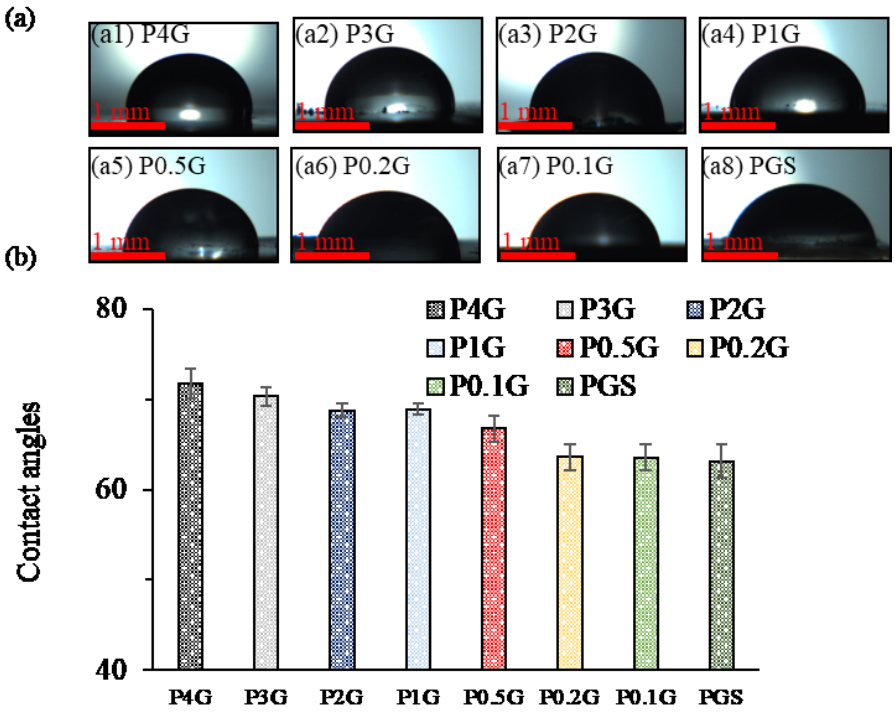

Fig. 3.2. Surface wettability of PGS-GnPs nanocomposites and elastomer. Optical images (a) represent the contact angles of water droplets on the top surface of samples in the order of 4 wt.%, 3 wt.%, 2 wt.%, 1 wt.%, 0.5 wt.%, 0.2 wt.%, and 0.1 wt.% of GnPs, and PGS elastomer from left to right respectively, (b) indicate the values of measured contact angles of each sample.

Fig. 3.2 shows the surface wettability of PGS-GnPs nanocomposites and elastomer. From the optical images of the water droplet on the surface of samples, shown in Fig. 3.2(a), we found the water droplet on the PGS surface has the largest spreading area and lowest height, while water droplets show reduced spreading area as the GnPs contents increasing. The contact angles of water droplets are measured and plotted in Fig. 3.2(b), which indicates increasing values from 63.2 ± 1.6° (PGS) to 63.4 ± 1.4° (0.1 wt.% GnPs), 63.8 ± 1.5° (0.2 wt.% GnPs), 66.8 ± 1.5° (0.5 wt.% GnPs), 68.8 ± 1.1° (1 wt.% GnPs), and 68.9 ± 1.6° (2 wt.% GnPs), 70.5 ± 1.1° (3 wt.% GnPs), and 72.1 ± 1.5° (4 wt.% GnPs). This could be attributed to the hydrophilicity of GnPs.

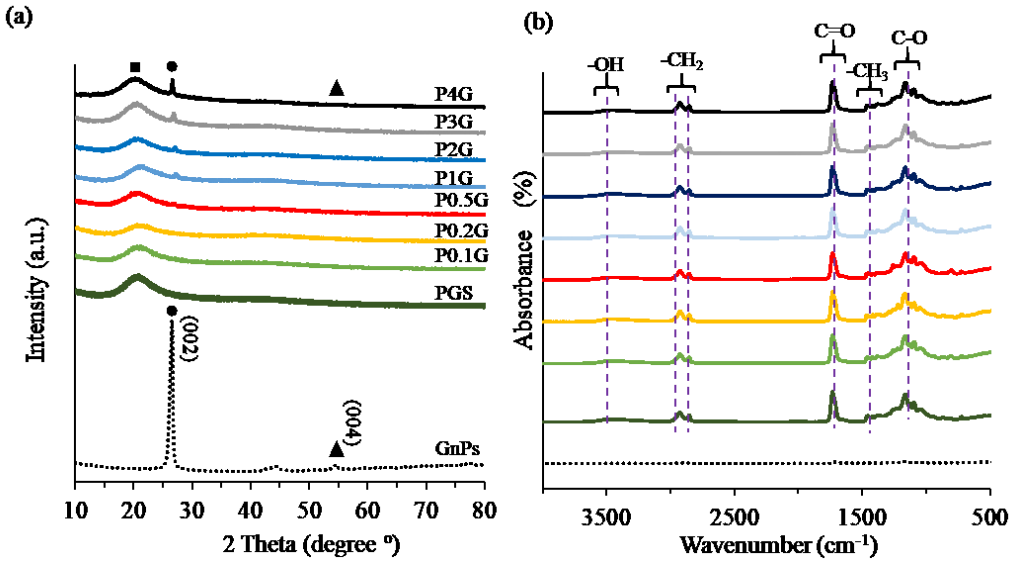

Fig. 3.3. Phase composition and chemical bonding of PGS-GnPs nanocomposite, GnPs, and PGS elastomer. (a) XRD spectrum and (b) FTIR spectrum of PGS-GnPs nanocomposite, GnPs, and PGS elastomer, respectively. In XRD plots, the black dots "●" indicate the GnPs peaks at 2θ ~ 26.5° which corresponds to the d002 plane, and the black triangles "▲" indicate GnPs peak at 2θ ~ 54.6° (d004). The black squares "■" indicate wide diffractions of PGS from 15° to 23.6° with a peak at 2θ of 20.8°. In FTIR plots, (1) 3500-3200 cm^{-1}, hydroxyl (–OH) group; (2) 2927–2852 cm^{-1}, alkene ($–CH_2$) group; (3) and (4) at 1735 and 1159 cm^{-1} were ester group(C=O and C–O. (5) 1354–1456 cm^{-1}, methyl ($–CH_3$) bending.

3.3.2. Crystallinity, Chemical bondings, and Cross-linking

The crystallinity of PGS-GnPs nanocomposites and PGS elastomer were identified as XRD spectrum, as shown in Fig. 3.3(a). PGS elastomer has a broad peak around 2θ = 21°, which indicated PGS elastomer has low crystallinity. GnPs show a characteristic peak at 2θ = 26.5° which corresponds to the plane (d002) of the exfoliated graphite nanoplatelets and another one at 2θ = 54.6° (d004) of graphite. Those two peaks were also observed in PGS-GnPs nanocomposites, and their intensities are enhanced as GnPs content increases.

3.3.3. Thermal Characterization

The thermal degradation of the elastomer occurs in a single step, starting at 250 °C and ending near 500 °C, as shown in Fig. 3.4(a). Fig. 3.4(b) shows the DSC curves of PGS–GnPs nanocomposites and pristine elastomer. The glass transition temperature (T_g) and melting temperature (T_m) during heating cycles and crystallization temperature (T_c) during cooling cycles were observed.

The PGS elastomeric matrix showed a glass transition temperature (T_g) approximately at −25 °C, followed by melting with maxima at −12 °C (Figure 3.3(e)), and both thermal transitions were not significantly affected by the incorporation of the conductive nanofiller. The presence of the GnPs had a significant effect on the crystallization of the PGS materials. Upon addition of the GnPs, there was a general shift of the melting and recrystallization peaks toward lower temperatures indicating a reduction in the purity of the crystals. In addition, the transition region became broader and the

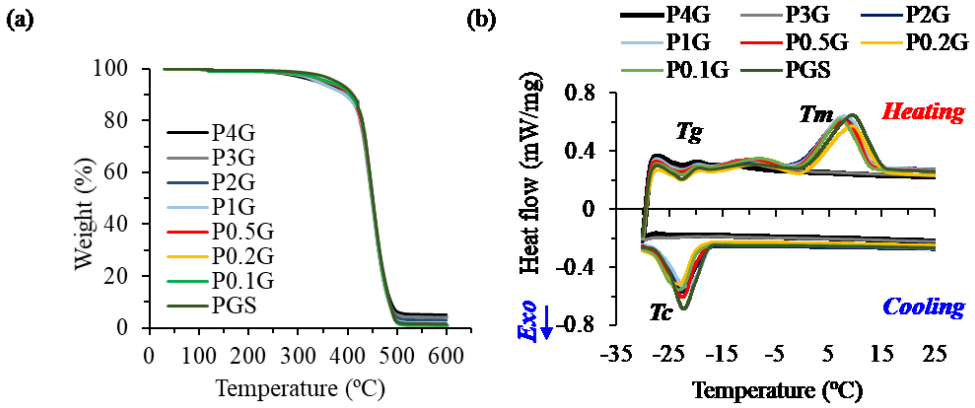

Fig. 3.4. Thermal properties of PGS-GnPs nanocomposites and pristine elastomer. (a) Thermogravimetric profiles and (b) differential scanning calorimetry curves of PGS-GnPs nanocomposites and pristine elastomer. The TGA curve indicated a decomposition temperature starting slowly from 300 °C, and the DSC curves revealed a glass transition around −22 °C, followed by a melting transition of around 10 °C.

melting and recrystallization energies decreased with the addition of GnPs showing that the percentage crystallinity in the material was reduced [37].

During the cooling DSC experiments, the recrystallization process occurred in a similar temperature region to the glass transition and so overlapped it. The endothermic peaks between −10 and 10 °C of heating cycles and exothermic peaks at approximately −20 °C of cooling cycles indicated that the PGS and PGS–GnPs nanocomposite materials are semicrystalline below Tm but soft and amorphous at the body temperature of 37 °C.

3.3.4. Mechanical Properties of PGS Elastomer and PGS-GnPs Nanocomposites

The mechanical behavior of the PGS-GnPs specimen was evaluated via uniaxial tensile load-extension tests, and the stress-strain curves were shown in Fig. 3.5.

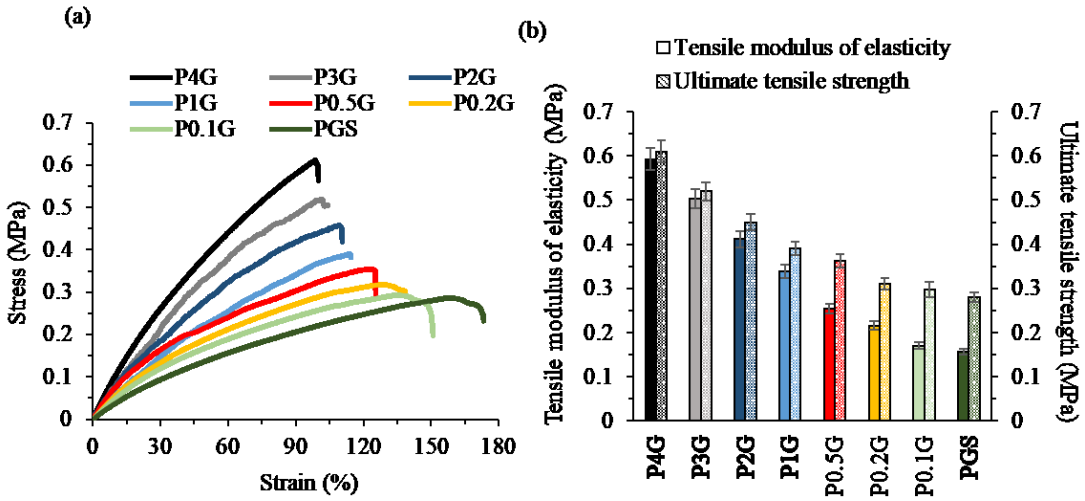

Fig. 3.5. Mechanical strength characterization of PGS-GnPs nanocomposites and pristine elastomer. (a) Stress-strain curves during tensile loading, and (b) the modulus of elasticity and ultimate tensile strength of PGS-GnPs nanocomposites and pristine elastomer, respectively. The modulus of elasticity was determined using Hooke's law from the slope of the linear portion of the stress-strain curve, whereas the UTS was determined as the highest stress that a nanofiber sample could bear without breaking.

Linear elastic deformation is observed for all PGS-GnPs nanocomposite and PGS elastomer. The PGS elastomer shows approximately 172 % elongations up to the breaking point, as shown in Fig. 3.5(a). It presents the *E* and *UTS* values of 0.16 ± 0.04 MPa and 0.29 ± 0.03 MPa, respectively, as shown in Fig. 3.5(b). As comparisons, the GnPs dopants reduce the elongation values to 98.7% (4 wt.% GnPs), 102.3% (3 wt.% GnPs), 108.6% (2 wt.% GnPs), 118.4% (1 wt.% GnPs), 123.2% (4 wt.% GnPs), 128.8% (0.5 wt.% GnPs), 132.5% (0.2 wt.% GnPs) and 144.5% (0.1% GnPs) strain, respectively.

Fig. 3.4(b) plots are the tensile modulus of elasticity (*E*) and ultimate tensile strength (*UTS*) of PGS-GnPs nanocomposites and elastomer. The incorporation of GnPs

significantly improved the *E* and *UTS* values from 0.59 ± 0.05 MPa and 0.61 ± 0.08 MPa (4 wt.% GnPs), 0.5 ± 0.3 MPa and 0.52 ± 0.03 MPa (3 wt.% GnPs), 0.41 ± 0.02 MPa and 0.45 ± 0.05 MPa (2 wt.% GnPs), 0.34 ± 0.03 MPa and 0.39 ± 0.02 MPa (1 wt.% GnPs), 0.25 ± 0.03 MPa and 0.36 ± 0.03 MPa (0.5 wt.% GnPs), 0.21 ± 0.03 MPa and 0.31± 0.03 MPa (0.2 wt.% GnPs), and 0.17 ± 0.02 MPa and 0.29 ± 0.02 MPa (0.1 wt.% GnPs), respectively.

3.3.5. Analyze Cytocompatibility of PGS-GnPs Nanocomposites with BMSCs

The morphology of BMSCs which are directly and indirectly contacted on PGS elastomer and PGS-GnPs nanocomposites were characterized using fluorescence microscopy, as shown in Fig. 3.6. BMSCs cultured in DMEMs and reference of glass showed healthy morphology. For direct contact, the BMSCs on the PGS elastomer appeared normal and showed hexagonal shapes and large spreading areas. While most of the cells on PGS-GnPs nanocomposite (1 wt.%, 0.5 wt.%, 0.2 wt.%, and 0.1 wt.% GnPs) showed healthy and normal morphology, a few cells exhibited long and slender shapes. In comparison, most of the BMSCs on the surface of PGS-GnPs nanocomposite (more than 1 wt. % of GnPs) showed abnormal morphology, slender shapes, and smaller spreading area. For BMSCs which are indirectly contacted with samples, most of them appeared normal morphology, while cells of PGS-GnPs nanocomposites with 2 wt.%, 3 wt.%, and 4 wt.% GnPs showed small spreading areas and abnormal shapes.

The BMSC adhesion density was quantified based on the fluorescence images, as shown in Fig. 3.7(a). For BMSCs directly contacted with samples at 24 h, the average cell

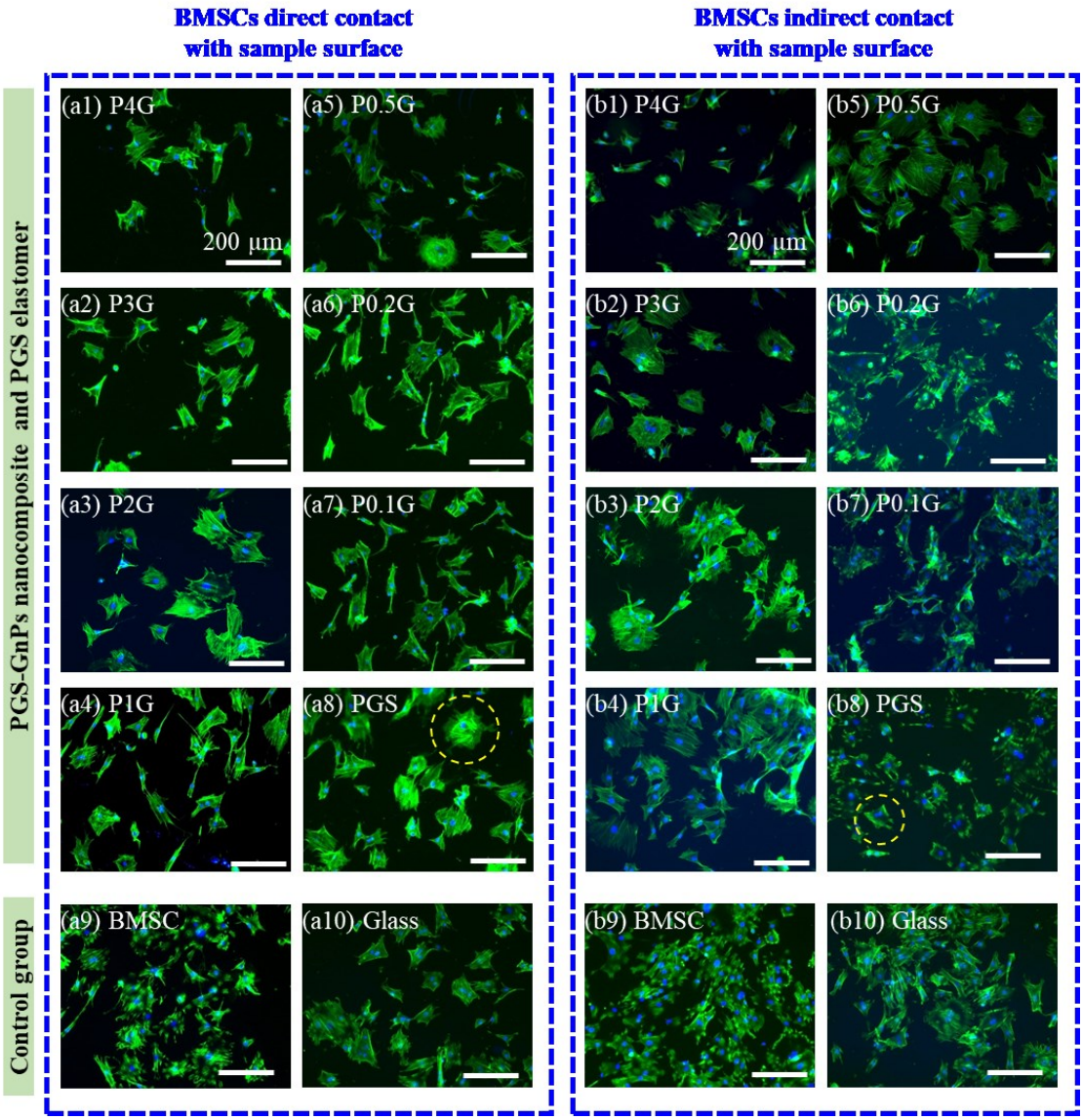

Fig. 3.6. Cell cytocompatibility analysis of BMSC and PGS-GnPs nanocomposites and elastomer. (a) and (b) indicated the fluorescence images of BMSC adhesion and morphology on the surfaces of samples and controls (direct contact) and on the surface of the well plate surrounding the samples and controls (indirect contact) after in vitro culture for 24 h. The original magnification is 100x, The scale bar is 200 μm. F-actin of BMSCs has been stained with Alexa Fluor 488 phalloidin as indicated in green color. BMSCs nucleus was stained with DAPI as indicated in blue color.

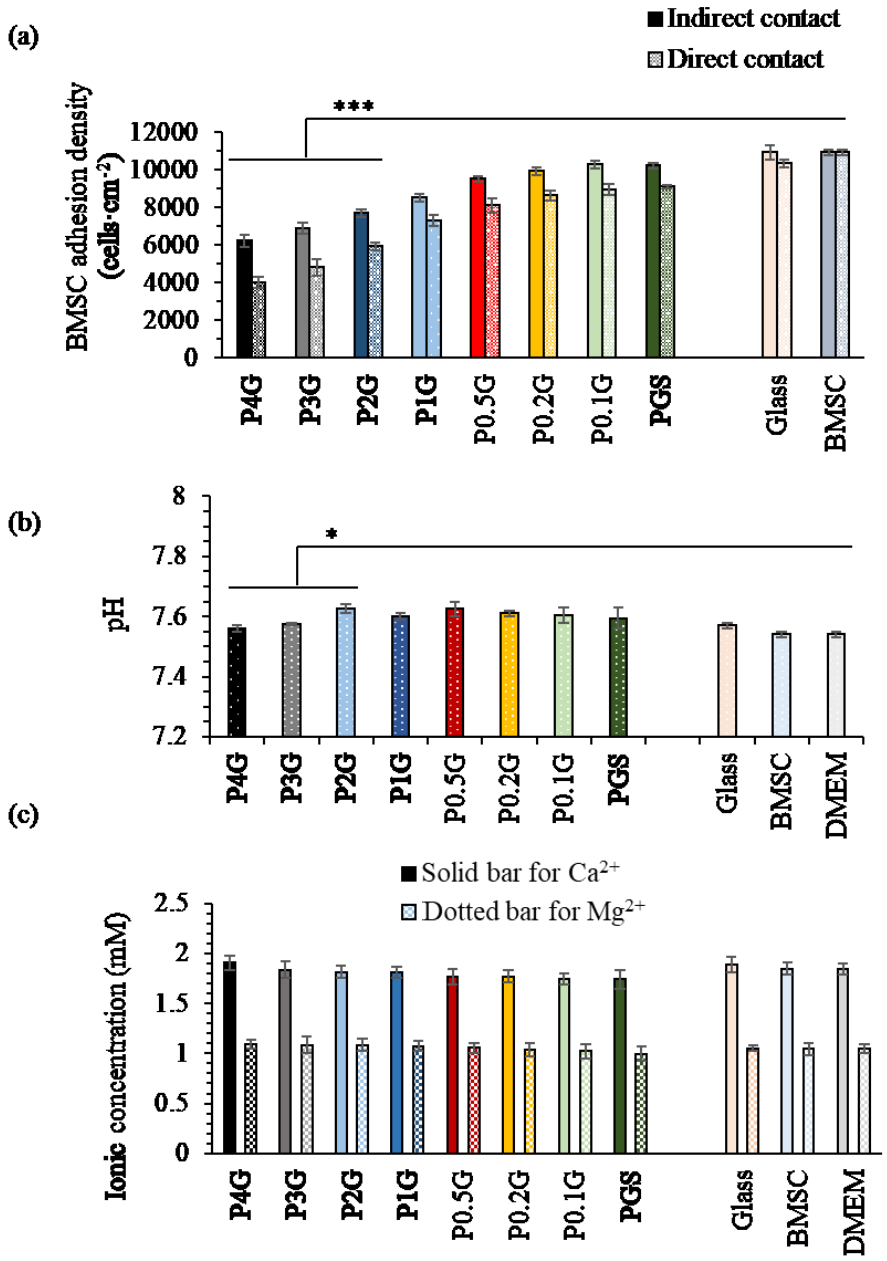

Fig. 3.7. Quantitative analyses of adhesion of BMSCs and post-culture media analysis. (a) adhesion density of BMSCs under indirect contact and direct contact conditions. (b) pH and (c) Ca^{2+} ion and Mg^{2+} ion concentrations and in the media after 24-h direct culture of BMSCs with the samples and controls. The values of pH and ion concentrations were the average of media of triple wells. *$p < 0.05$, **$p < 0.01$, ***$p < 0.001$ when compared with the BMSC control.

adhesion densities of glass and BMSC controls were 10.3×10^4 and 10.9×10^3 cells/cm^2 respectively. While the BMSCs on the surface of the PGS elastomer showed average cell adhesion densities of 9.1×10^3 cells/cm^2. As a compersion, the PGS-GnPs nanocomposite samples possess lower BMSCs adhesion densities, especially for samples with higher than 1 wt.% of GnPs contents showed statistical significance. For BMSCs indirectly contacted with samples at 24 h, the average cell adhesion densities are generally higher than those values of direct contact and statistical significance was observed between samples with higher than 1 wt.% of GnPs contents and BMSCs controls.

To evaluate the influence of degradation and hydrolysis products of PGS-GnPs nanocomposites and PGS elastomer on the pH and ion concentrations, the post-culture media were measured and plotted in Fig. 3.7(b) and (c). The acidic product of PGS hydrolysis could reduce the pH value. The Mg^{2+} and Ca^{2+} concentrations of PGS-GnPs nanocomposite showed an increasing trend as the GnPs contents increased. The control glass and BMSCs showed Mg^{2+} concentrations of 1.05 ± 0.4 and 1.04 ± 0.3 mM, and the PGS elastomer showed an Mg^{2+} concentration value of 0.99 ± 0.3 mM, while the sample with 20 wt.% GnPs possess Mg^{2+} concentration value of 1.07 ± 0.5 mM. For Ca^{2+} concentrations, The control glass and BMSCs showed Ca^{2+} concentrations of 1.88 ± 0.6 and 1.84 ± 0.5 mM, and the PGS elastomer showed a decreased value of Ca^{2+} concentration to 1.74 ± 0.6 mM, while the sample with 20 wt.% GnPs possess Ca^{2+} concentration value of 1.9 ± 0.6 mM. There is no statistical significance observed.

3.3.4. DISCUSSION

3.4.1. Effect of GnPs on the Cross-linking of PGS Nanocomposites

PGS elastomer shows smooth morphology on cross-section and top surface, which is consistent with others' reports [28]. The GnPs dopants are very uniformly dispersed in the PGS matrix. With high GnPs contents (4 wt.%, 3 wt.%, and 2 wt.%), the GnPs forms interconnected network and agglomerates in PGS. Very few agglomerates were found on the sample with less than 1 wt.% GnPs. The agglomerate work as defects in the polymer matrix, facilitating crack initiation during mechanical deformation [103]. Similar appearances were also found in poly(lactic acid) (PLA) and GnPs nanocomposite [48, 55, 56]. The presence of GnPs on the surface greatly affects the wettability of samples and increases the hydrophobic effects, which were observed in others' reports [58, 59]. From the XRD spectrum Fig. 3.3(a), there is no shift with GnPs' peak, which indicates that GnPs maintained intact platelets spacing and structure in the matrix. The wide peaks of PGS didn't change which shows that GnPs dopants didn't affect the crystallinity of the PGS matrix. Higher GnPs contents in PGS-GnPs nanocomposites possess higher crystallinity degrees, which results in higher tensile modulus of elasticity but lower elongations to rupture. The enhancement could be attributed to the chemical bonding and physical interactions between GnPs functional groups and PGS chains.

3.4.2. Influence of GnPs on the Biological Properties

The PGS-GnPs nanocomposites have increased the hydrophilicity with rising GnPs contents. The larger water contact angles of PGS-GnPs nanocomposites, as shown in Fig.

3.2, would inhibit the adhesion of BMSCs on the sample surface and the depositions of Mg and Ca ions of the cell media. Studies on Gr and GnPs cytocompatibility from published research showed controversial results. In our study, the GnPs showed dose-dependent toxicity on BMSCs with a threshold of approximately 1 wt.% GnPs contents. Similar results were found for PLA-GnPs nanocomposite with fibroblasts [103] and polyethylene-GnPs nanocomposite with osteoblast [104]. The fluorescence images (Fig. 3.6) indicated that BMSCs attached to the surface of the sample (4 wt.%, 3 wt.%, 2 wt.%, and 1 wt.% of GnPs) were reduced in numbers and spreading areas. Some researchers found that Gr has no effect on the viability of PC12 neural cells within a concentration of 0.01−10 μg/mL [105]. The mechanisms of cytotoxicity with different cell types for Gr and GnPs materials could own to physical damage or disruption of the cell membrane [106] and cytoskeleton[107], reactive oxygen species (ROS) [108], and other DNA or chromosome damage [109]. The big clusters of GnPs at higher concentrations can attach to BMSCs easily on their surface and the sharp contact at cleavages and edges of Gr membranes could lead to membrane rupture and cell death.

3.5. CONCLUSION

In this study, PGS-GnPs nanocomposites with GnPs contents ranging from 4 wt.% to 0.1 wt.% were synthesized using solvent casting methods. The GnPs dopants showed great influence on the physicochemical properties of nanocomposites. The tensile modulus of elasticity and ultimate tensile strength of PGS-GnPs nanocomposites were enhanced with various amounts of GnPs dopants. Meanwhile, the nanocomposites with low contents of GnPs dopants show good cytocompatibility with BMSCs after 24 h cell cultures. These

findings demonstrate that PGS-GnPs nanocomposites with proper GnPs would be suitable for tissue and stem cell applications.

3.6. ACKNOWLEDGMENT

The authors would like to thank the University of California at Riverside for financial support the authors thank the Central Facility for Advanced Microscopy and Microanalysis (CFAMM) at the UC-Riverside for the use of SEM/EDS. The training of instruments from labmates and managers.

CONCLUSION

This project presented here focused on developing novel nanocomposites and exploring promising biomedical applications, such as tissue engineering scaffolds for nerve guidance conduits and bone regeneration scaffolds, and wearable sensors for physiological and motion signal monitoring.

The study of triphasic nanocomposite explored the effect of nanoparticles on crosslinking density of PGS elastomer and dose-dependent toxicity with BMSCs. Meanwhile, the BMSCs cell study result indicated that the surface patterns have shown excellent guidance of BMSCs alignment. Also, we observed that GnPs could greatly reduce the electrical resistance of nanocomposites. We identified the formation of the magnesium carboxylate complex in the nanocomposite from the FTIR-ATR spectrum, which signification enhanced the crosslinking density of PGS matrice.

Thus, we further investigated the biphasic nanocomposites by incorporating various GnPs content (from 25 wt.% to 0.1 wt.%) into the PGS elastomer matrix. We found a percolation threshold for conductive PGS-GnPs nanocomposites at approximately 10 wt.% of GnPs. The conductive PGS-GnPs nanocomposites showed good piezoresistive behaviors which have promising potential in wearable and flexible sensor. Our PGS-GnPs nanocomposites with different GnPs contents exhibited different GF values under various strains up to 30%. , thus could be applied as strain sensors in movements with different deformations, such as finger motion (small strain) and knee joint motion (large strain). Meanwhile, the GF factor with a value up to 61.7 is stable and reliable, which is much more sensitive than other results.

In addation, we observed that the GnPs dopants exhibited dose-dependant toxic and adverse effects on BMSCs adherence with more 1 wt.% concentrations of GnPs. The PGS-GnPs nanocomposites with less than 1 wt.% concentrations of GnPs showed good cytocompatibility. Meanhile, their mechanical properties match the strength of human tissues, which could be potentially employed for tissue engineering scaffolds. The special surface morphology of PGS-GnPs nanocomposite would be promising to provide local electrons transfer and electrical stimulus. These composites with low GnPs contents would be promising to facilitate the differentiation of neural stem cells into nerons in nerve repair applications. Compared with current conductive polymers, which are non-degradable, PGS-GnPs nanocomposites also showed advantages with full degradabilities.

Bibliography

1. Muhammed Shameem, M., et al., *A brief review on polymer nanocomposites and its applications.* Materials Today: Proceedings, 2021. 45: p. 2536-2539.
2. Akpan, E.I., et al., *Design and Synthesis of Polymer Nanocomposites*, in *Polymer Composites with Functionalized Nanoparticles*. 2019. p. 47-83.
3. Mansor, M.R. and M.Z. Akop, *Polymer nanocomposites smart materials for energy applications*, in *Polymer nanocomposite-Based smart materials*. 2020, Elsevier. p. 157-176.
4. Gupta, T.K. and S. Kumar, *Fabrication of carbon nanotube/polymer nanocomposites*, in *Carbon Nanotube-Reinforced Polymers*. 2018, Elsevier. p. 61-81.
5. Boakye, M.A.D., et al., *Fabrication and Characterization of Electrospun PCL-MgO-Keratin-Based Composite Nanofibers for Biomedical Applications.* Materials (Basel), 2015. 8(7): p. 4080-4095.
6. Zhao, Y., et al., *The Degradation Properties of MgO Whiskers/PLLA Composite In Vitro.* Int J Mol Sci, 2018. 19(9).
7. Wang, W., et al., *Conductive Polymer-Inorganic Hybrid Materials through Synergistic Mutual Doping of the Constituents.* ACS Appl Mater Interfaces, 2017. 9(33): p. 27964-27971.
8. Vinayak, G.K., et al., *Synthesis, Characterization and DC Conductivity Studies on Polyaniline/ZnO Composites.* Ferroelectrics, 2015. 486(1): p. 106-113.

9. Makhluf, S., et al., *Microwave-Assisted Synthesis of Nanocrystalline MgO and Its Use as a Bacteriocide.* Advanced Functional Materials, 2005. 15(10): p. 1708-1715.

10. Koper, O.B., et al., *Nanoscale Powders and Formulations with Biocidal Activity Toward Spores and Vegetative Cells of Bacillus Species, Viruses, and Toxins.* Current Microbiology, 2002. 44(1): p. 49-55.

11. Stoimenov, P.K., et al., *Metal Oxide Nanoparticles as Bactericidal Agents.* Langmuir, 2002. 18(17): p. 6679-6686.

12. Venugopal, G., et al., *Structural and Mechanical Properties of MgO-Poly(Vinyl Alcohol) Nanocomposite Film.* Advanced Science, Engineering and Medicine, 2015. 7(6): p. 457-464.

13. Qian, Y., et al., *An integrated multi-layer 3D-fabrication of PDA/RGD coated graphene loaded PCL nanoscaffold for peripheral nerve restoration.* Nat Commun, 2018. 9(1): p. 323.

14. Wang, Y., et al., *A tough biodegradable elastomer.* 2002. 20(6): p. 602.

15. Chen, Q.Z., et al., *Characterisation of a soft elastomer poly(glycerol sebacate) designed to match the mechanical properties of myocardial tissue.* Biomaterials, 2008. 29(1): p. 47-57.

16. Sundback, C.A., et al., *Biocompatibility analysis of poly(glycerol sebacate) as a nerve guide material.* Biomaterials, 2005. 26(27): p. 5454-64.

17. Hu, Y., et al., *3D-engineering of Cellularized Conduits for Peripheral Nerve Regeneration.* Sci Rep, 2016. 6: p. 32184.

18. Shahriari, D., et al., *Peripheral nerve growth within a hydrogel microchannel scaffold supported by a kink-resistant conduit.* J Biomed Mater Res A, 2017. 105(12): p. 3392-3399.

19. Georgiou, M., et al., *Engineered neural tissue for peripheral nerve repair.* Biomaterials, 2013. 34(30): p. 7335-43.

20. Wetteland, C.L., N.Y. Nguyen, and H. Liu, *Concentration-dependent behaviors of bone marrow derived mesenchymal stem cells and infectious bacteria toward magnesium oxide nanoparticles.* Acta Biomater, 2016. 35: p. 341-56.

21. Rijal, N.P., et al., *Magnesium oxide-poly(ε-caprolactone)-chitosan-based composite nanofiber for tissue engineering applications.* Materials Science and Engineering: B, 2018. 228: p. 18-27.

22. Pasquet, J., et al., *The contribution of zinc ions to the antimicrobial activity of zinc oxide.* Colloids and Surfaces A: Physicochemical and Engineering Aspects, 2014. 457: p. 263-274.

23. Reddy, L.S., et al., *Antimicrobial activity of zinc oxide (ZnO) nanoparticle against Klebsiella pneumoniae.* Pharm Biol, 2014. 52(11): p. 1388-97.

24. Jeng, H.A. and J. Swanson, *Toxicity of metal oxide nanoparticles in mammalian cells.* J Environ Sci Health A Tox Hazard Subst Environ Eng, 2006. 41(12): p. 2699-711.

25. Zou, Y., et al., *Synthesis and cellular compatibility of Co-doped ZnO particles in silk-fibroin peptides.* Colloids Surf B Biointerfaces, 2013. 102: p. 29-36.

26. Tadyszak, K., J.K. Wychowaniec, and J. Litowczenko, *Biomedical Applications of Graphene-Based Structures.* Nanomaterials (Basel), 2018. 8(11).

27. Ryu, S. and B.-S. Kim, *Culture of neural cells and stem cells on graphene.* Tissue Engineering and Regenerative Medicine, 2013. 10(2): p. 39-46.

28. Zhang, X., et al., *Porous poly(glycerol sebacate) (PGS) elastomer scaffolds for skin tissue engineering.* Polymer Testing, 2016. 54: p. 118-125.

29. Kerativitayanan, P. and A.K. Gaharwar, *Elastomeric and mechanically stiff nanocomposites from poly(glycerol sebacate) and bioactive nanosilicates.* Acta Biomater, 2015. 26: p. 34-44.

30. Cai, W. and L. Liu, *Shape-memory effect of poly (glycerol–sebacate) elastomer.* Materials Letters, 2008. 62(14): p. 2171-2173.

31. Abudula, T., et al., *The Effect of Poly (Glycerol Sebacate) Incorporation within Hybrid Chitin-Lignin Sol-Gel Nanofibrous Scaffolds.* Materials (Basel), 2018. 11(3).

32. Ansari, A., et al., *Microwave-assisted MgO NP catalyzed one-pot multicomponent synthesis of polysubstituted steroidal pyridines.* New Journal of Chemistry, 2018. 42(1): p. 184-197.

33. Gandhi, S., et al., *Synthesis and characterizations of nano sized MgO and its nano composite with poly(vinyl alcohol).* Journal of Non-Crystalline Solids, 2011. 357(1): p. 181-185.

34. Niu, H., et al., *Large-scale synthesis of single-crystalline MgO with bone-like nanostructures.* Journal of Nanoparticle Research, 2006. 8(6): p. 881-888.

35. Liang, S.-L., et al., *The mechanical characteristics and in vitro biocompatibility of poly (glycerol sebacate)-Bioglass® elastomeric composites.* Biomaterials, 2010. 31(33): p. 8516-8529.

36. Kim, D.H., et al., *Effect of Immobilized Nerve Growth Factor on Conductive Polymers: Electrical Properties and Cellular Response.* Advanced Functional Materials, 2007. 17(1): p. 79-86.

37. Liang, S., W.D. Cook, and Q. Chen, *Physical characterization of poly(glycerol sebacate)/Bioglass® composites.* Polymer International, 2012. 61(1): p. 17-22.

38. Apatiga, J.L., et al., *Non-Covalent Interactions on Polymer-Graphene Nanocomposites and Their Effects on the Electrical Conductivity.* Polymers (Basel), 2021. 13(11).

39. del Castillo, R.M., et al., *Experimental and computational conductivity study of multilayer graphene in polypropylene nanocomposites.* Journal of Materials Chemistry C, 2018. 6(27): p. 7232-7241.

40. Hu, Y., J.O. You, and J. Aizenberg, *Micropatterned Hydrogel Surface with High-Aspect-Ratio Features for Cell Guidance and Tissue Growth.* ACS Appl Mater Interfaces, 2016. 8(34): p. 21939-45.

41. Sun, B., et al., *Preferred cell alignment along concave microgrooves.* RSC Advances, 2017. 7(11): p. 6788-6794.

42. Hu, J., et al., *Enhanced cell adhesion and alignment on micro-wavy patterned surfaces.* PLoS One, 2014. 9(8): p. e104502.

43. Cipriano, A.F., et al., *Bone marrow stromal cell adhesion and morphology on micro- and sub-micropatterned titanium.* J Biomed Nanotechnol, 2014. 10(4): p. 660-8.

44. Petas, A., et al., *Bacterial adherence to self-reinforced polyglycolic acid and self-reinforced polylactic acid 96 urological spiral stents in vitro.* Biomaterials, 1998. 19(7-9): p. 677-681.

45. Jeong, C.G. and S.J. Hollister, *A comparison of the influence of material on in vitro cartilage tissue engineering with PCL, PGS, and POC 3D scaffold architecture seeded with chondrocytes.* Biomaterials, 2010. 31(15): p. 4304-12.

46. Crapo, P.M., J. Gao, and Y. Wang, *Seamless tubular poly(glycerol sebacate) scaffolds: high-yield fabrication and potential applications.* J Biomed Mater Res A, 2008. 86(2): p. 354-63.

47. Gadomska-Gajadhur, A., et al., *Optimization of Poly(glycerol sebacate) Synthesis for Biomedical Purposes with the Design of Experiments.* Organic Process Research & Development, 2018. 22(12): p. 1793-1800.

48. Kashi, S., et al., *Morphology, electromagnetic properties and electromagnetic interference shielding performance of poly lactide/graphene nanoplatelet nanocomposites.* Materials & Design, 2016. 95: p. 119-126.

49. Li, Y., et al., *Poly(propylene)/Graphene Nanoplatelet Nanocomposites: Melt Rheological Behavior and Thermal, Electrical, and Electronic Properties.* Macromolecular Chemistry and Physics, 2011. 212(18): p. 1951-1959.

50. Kalakonda, P., et al., *Microfibrous silver-coated polymeric scaffolds with tunable mechanical properties.* RSC Advances, 2017. 7(55): p. 34331-34338.

51. Frydrych, M., et al., *Biomimetic poly(glycerol sebacate)/poly(l-lactic acid) blend scaffolds for adipose tissue engineering.* Acta Biomater, 2015. 18: p. 40-9.

52. Jaafar, I.H., et al., *Spectroscopic evaluation, thermal, and thermomechanical characterization of poly(glycerol-sebacate) with variations in curing temperatures and durations.* Journal of Materials Science, 2010. 45(9): p. 2525-2529.

53. Liang, S.L., et al., *In vitro enzymatic degradation of poly (glycerol sebacate)-based materials.* Biomaterials, 2011. 32(33): p. 8486-96.

54. Ghorbani, M.M. and R. Taherian, *Methods of Measuring Electrical Properties of Material*, in *Electrical Conductivity in Polymer-Based Composites: Experiments, Modelling and Applications*. 2019. p. 365-394.

55. Spitalsky, Z., et al., *Carbon nanotube–polymer composites: Chemistry, processing, mechanical and electrical properties.* Progress in Polymer Science, 2010. 35(3): p. 357-401.

56. Narimissa, E., et al., *Melt rheological investigation of polylactide -nanographite platelets biopolymer composites.* Polymer Engineering & Science, 2014. 54(1): p. 175-188.

57. Guo, Q., et al., *A well-organized graphene nanostructure for versatile strain-sensing application constructed by a covalently bonded graphene/rubber interface.* Journal of Materials Chemistry C, 2018. 6(8): p. 2139-2147.

58. Pinto, A.M., et al., *Biocompatibility of poly(lactic acid) with incorporated graphene-based materials.* Colloids Surf B Biointerfaces, 2013. 104: p. 229-38.

59. Wang, J., et al., *Preparation of graphene/poly (vinyl alcohol) nanocomposites with enhanced mechanical properties and water resistance.* Polymer International, 2011. 60(5): p. 816-822.

60. Gorrasi, G., et al., *Carbon nanotube induced structural and physical property transitions of syndiotactic polypropylene.* Nanotechnology, 2007. 18(27).

61. Ku-Herrera, J.J. and F. Avilés, *Cyclic tension and compression piezoresistivity of carbon nanotube/vinyl ester composites in the elastic and plastic regimes.* Carbon, 2012. 50(7): p. 2592-2598.

62. Chang, J., et al., *The production of carbon nanotube/epoxy composites with a very high dielectric constant and low dielectric loss by microwave curing.* Carbon, 2012. 50(2): p. 689-698.

63. Yan, C., et al., *Highly stretchable piezoresistive graphene-nanocellulose nanopaper for strain sensors.* Adv Mater, 2014. 26(13): p. 2022-7.

64. Kong, J.-H., et al., *Simple and rapid micropatterning of conductive carbon composites and its application to elastic strain sensors.* Carbon, 2014. 77: p. 199-207.

65. Wang, B., et al., *Graphene/polydimethylsiloxane nanocomposite strain sensor.* Review of Scientific Instruments, 2013. 84(10): p. 105005.

66. Yamada, T., et al., *A stretchable carbon nanotube strain sensor for human-motion detection.* Nat Nanotechnol, 2011. 6(5): p. 296-301.

67. Guo, D., et al., *Effects of service condition on the performance of conductive polymer composites for flexible strain sensors.* Sensors and Actuators A: Physical, 2021. 318.

68. Sencadas, V., C. Tawk, and G. Alici, *Highly Sensitive Soft Foam Sensors to Empower Robotic Systems.* Advanced Materials Technologies, 2019. 4(10).

69. Faroni, A., et al., *Peripheral nerve regeneration: experimental strategies and future perspectives.* Adv Drug Deliv Rev, 2015. 82-83: p. 160-7.

70. Chhabra, A., et al., *Peripheral nerve injury grading simplified on MR neurography: as referenced to Seddon and Sunderland classifications.* The Indian journal of radiology & imaging, 2014. 24(3): p. 217.

71. Leung, Y.H., et al., *Mechanisms of antibacterial activity of MgO: non-ROS mediated toxicity of MgO nanoparticles towards Escherichia coli.* Small, 2014. 10(6): p. 1171-83.

72. Xie, J., et al., *Nerve guidance conduits based on double-layered scaffolds of electrospun nanofibers for repairing the peripheral nervous system.* ACS Appl Mater Interfaces, 2014. 6(12): p. 9472-80.

73. Szynkaruk, M., et al., *Experimental and clinical evidence for use of decellularized nerve allografts in peripheral nerve gap reconstruction.* Tissue Eng Part B Rev, 2013. 19(1): p. 83-96.

74. Deumens, R., et al., *Repairing injured peripheral nerves: Bridging the gap.* Prog Neurobiol, 2010. 92(3): p. 245-76.

75. Ortigiiela, M.E., M.B. Wood, and D.R. Cahill, *Anatomy of the sural nerve complex.* The Journal of Hand Surgery, 1987. 12(6): p. 1119-1123.

76. Mackinnon, S.E. and A.R. Hudson, *Clinical Application of Peripheral Nerve Transplantation.* Plastic and Reconstructive Surgery, 1992. 90(4): p. 695-699.

77. Zhang, L.G. and D.L. Kaplan, *Neural engineering: From advanced biomaterials to 3D fabrication techniques*. 2016: Springer.

78. Widmer, M.S., et al., *Manufacture of porous biodegradable polymer conduits by an extrusion process for guided tissue regeneration.* Biomaterials, 1998. 19(21): p. 1945-1955.

79. Lin, K.-M., et al., *Nerve growth factor released from a novel PLGA nerve conduit can improve axon growth.* Journal of Micromechanics and Microengineering, 2016. 26(4).

80. Reid, A.J., et al., *Long term peripheral nerve regeneration using a novel PCL nerve conduit.* Neurosci Lett, 2013. 544: p. 125-30.

81. Den Dunnen, W., et al., *Poly (DL-lactide-ϵ-caprolactone) nerve guides perform better than autologous nerve grafts.* Microsurgery: Official Journal of the International Microsurgical Society and the European Federation of Societies for Microsurgery, 1996. 17(7): p. 348-357.

82. Hsu, S.H., W.C. Chang, and C.T. Yen, *Novel flexible nerve conduits made of water-based biodegradable polyurethane for peripheral nerve regeneration.* J Biomed Mater Res A, 2017. 105(5): p. 1383-1392.

83. Robinson, P.H., et al., *Nerve regeneration through a two-ply biodegradable nerve guide in the rat and the influence of ACTH4-9 nerve growth factor.* Microsurgery, 1991. 12(6): p. 412-419.

84. Langone, F., et al., *Peripheral nerve repair using a poly (organo) phosphazene tubular prosthesis.* Biomaterials, 1995. 16(5): p. 347-353.

85. Schappacher, M., et al., *Study of a (trimethylenecarbonate-co-ε-caprolactone) polymer—Part 1: Preparation of a new nerve guide through controlled random copolymerization using rare earth catalysts.* Biomaterials, 2001. 22(21): p. 2849-2855.

86. Dahlin, L., *Techniques of peripheral nerve repair.* Scandinavian Journal of Surgery, 2008. 97(4): p. 310-316.

87. Manzanedo, D., *Biorubber (PGS): Evaluation of a novel biodegradable elastomer*. 2006, Massachusetts Institute of Technology.

88. Nectow, A.R., K.G. Marra, and D.L. Kaplan, *Biomaterials for the development of peripheral nerve guidance conduits.* Tissue Eng Part B Rev, 2012. 18(1): p. 40-50.

89. Rydevik, B.L., et al., *An in vitro mechanical and histological study of acute stretching on rabbit tibial nerve.* 1990. 8(5): p. 694-701.

90. McKee, C.T., et al., *Indentation versus tensile measurements of Young's modulus for soft biological tissues.* Tissue Eng Part B Rev, 2011. 17(3): p. 155-64.

91. Lee, M.-C. and R.C. Haut, *Strain rate effects on tensile failure properties of the common carotid artery and jugular veins of ferrets.* Journal of biomechanics, 1992. 25(8): p. 925-927.

92. Geim, A.K. and K.S. Novoselov, *The rise of graphene*, in *Nanoscience and technology: a collection of reviews from nature journals*. 2010, World Scientific. p. 11-19.

93. Zhu, Y., et al., *Graphene and graphene oxide: synthesis, properties, and applications.* Advanced materials, 2010. 22(35): p. 3906-3924.

94. Zhang, Y., S. Wang, and P. Yang, *Effects of Graphene-Based Materials on the Behavior of Neural Stem Cells.* Journal of Nanomaterials, 2020. 2020: p. 1-16.

95. Liao, K.-H., et al., *Cytotoxicity of graphene oxide and graphene in human erythrocytes and skin fibroblasts.* ACS applied materials & interfaces, 2011. 3(7): p. 2607-2615.

96. Sasidharan, A., et al., *Differential nano-bio interactions and toxicity effects of pristine versus functionalized graphene.* Nanoscale, 2011. 3(6): p. 2461-2464.

97. Akhavan, O., E. Ghaderi, and A. Akhavan, *Size-dependent genotoxicity of graphene nanoplatelets in human stem cells.* Biomaterials, 2012. 33(32): p. 8017-25.

98. Hong, S.W., et al., *Enhanced neural cell adhesion and neurite outgrowth on graphene-based biomimetic substrates.* Biomed Res Int, 2014. 2014: p. 212149.

99. Solanki, A., et al., *Axonal alignment and enhanced neuronal differentiation of neural stem cells on graphene-nanoparticle hybrid structures.* Adv Mater, 2013. 25(38): p. 5477-82.

100. Wang, Y., et al., *Fluorinated graphene for promoting neuro -induction of stem cells.* Advanced materials, 2012. 24(31): p. 4285-4290.

101. Park, S.Y., et al., *Enhanced differentiation of human neural stem cells into neurons on graphene.* Advanced materials, 2011. 23(36): p. H263-H267.

102. Bressan, E., et al., *Graphene based scaffolds effects on stem cells commitment.* J Transl Med, 2014. 12: p. 296.

103. Gonçalves, C., et al., *Biocompatible reinforcement of poly(Lactic acid) with graphene nanoplatelets.* Polymer Composites, 2018. 39: p. E308-E320.

104. Lahiri, D., et al., *Graphene nanoplatelet-induced strengthening of ultrahigh molecular weight polyethylene and biocompatibility in vitro.* ACS Appl Mater Interfaces, 2012. 4(4): p. 2234-41.

105. Zhang, Y., et al., *Cytotoxicity effects of graphene and single-wall carbon nanotubes in neural phaeochromocytoma-derived PC12 cells.* ACS nano, 2010. 4(6): p. 3181-3186.

106. Seabra, A.B., et al., *Nanotoxicity of graphene and graphene oxide.* Chem Res Toxicol, 2014. 27(2): p. 159-68.

107. Tian, X., et al., *Graphene Oxide Nanosheets Retard Cellular Migration via Disruption of Actin Cytoskeleton.* Small, 2017. 13(3).

108. Chen, M., et al., *Oxidative stress and immunotoxicity induced by graphene oxide in zebrafish.* Aquat Toxicol, 2016. 174: p. 54-60.

109. Fahmi, T., et al., *Mechanism of graphene-induced cytotoxicity: Role of endonucleases.* J Appl Toxicol, 2017. 37(11): p. 1325-1332.